Experimental investigation of premixed ammonia combustion at high Karlovitz number conditions

Fan, Qingshuang

2021

Document Version:
Publisher's PDF, also known as Version of record

Experimental investigation of premixed ammonia combustion at high Karlovitz number conditions

QINGSHUANG FAN
DEPARTMENT OF PHYSICS | FACULTY OF ENGINEERING | LUND UNIVERSITY

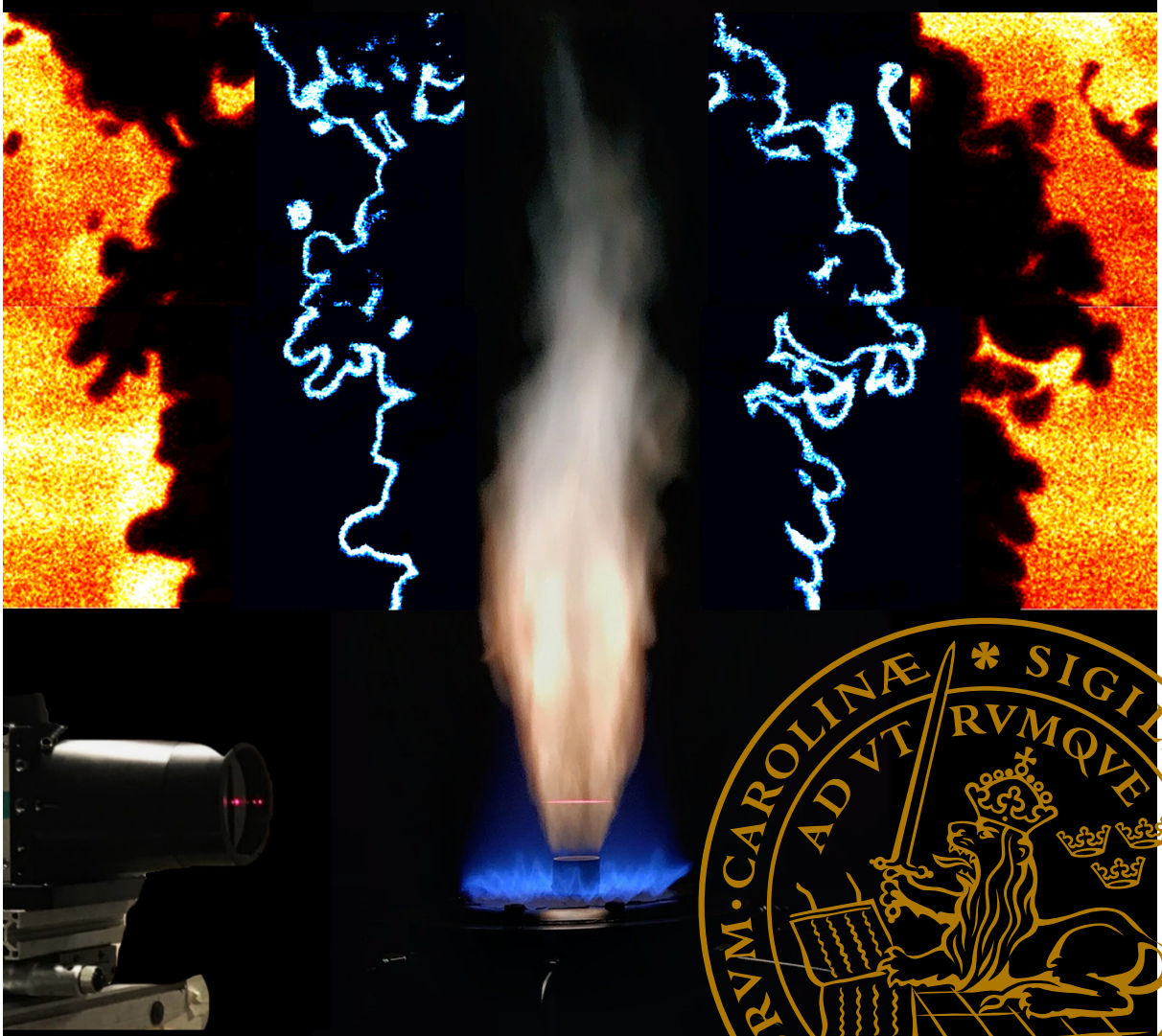

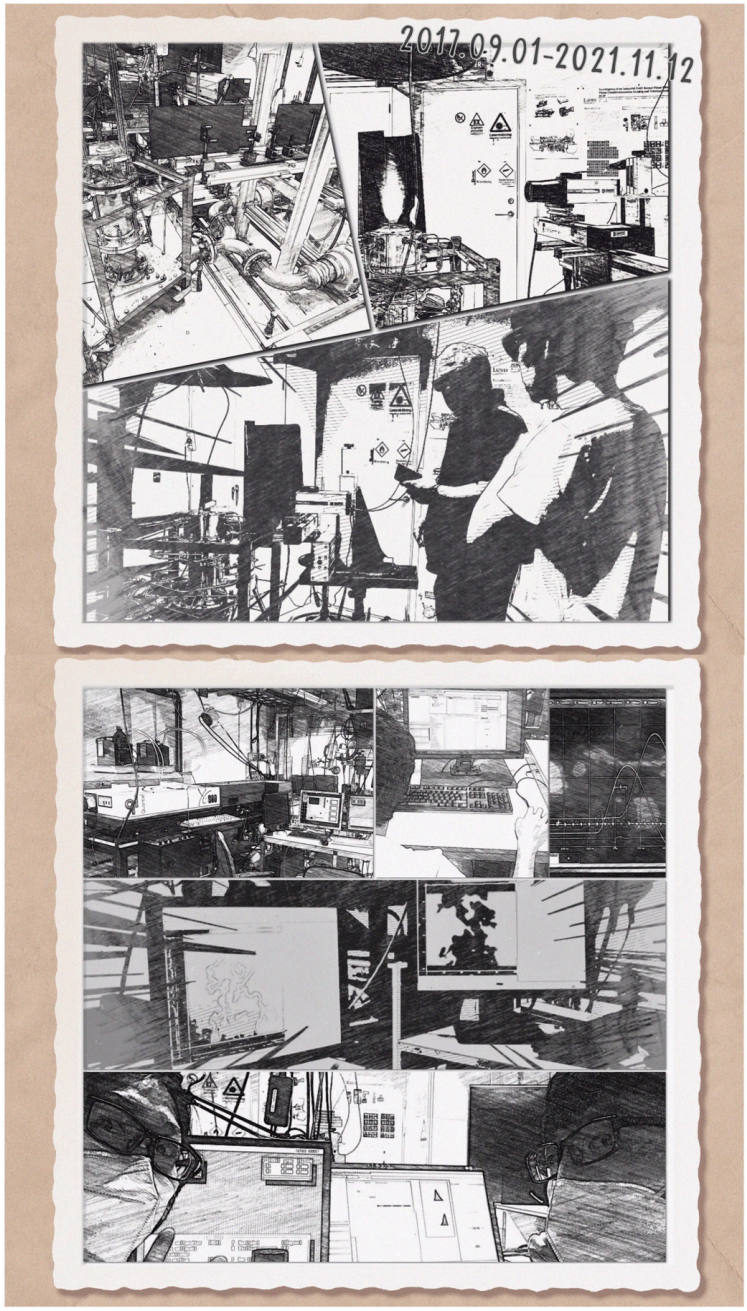

Printed by Media-Tryck, Lund 2021 NORDIC SWAN ECOLABEL 3041 0903

Faculty of Engineering
Department of Physics
Division of Combustion Physics

Lund Reports on Combustion Physics: LRCP-238 (2021)
ISRN LUTFD2/TFCP-238-SE
ISBN 978-91-8039-045-3
ISSN 1102-8718

LUND UNIVERSITY

Experimental investigation of premixed ammonia combustion at high Karlovitz number conditions

Experimental investigation of premixed ammonia combustion at high Karlovitz number conditions

Qingshuang Fan

LUND
UNIVERSITY

DOCTORAL DISSERTATION
by due permission of the Faculty of Engineering, Lund University, Sweden.
To be defended at Rydbergssalen, Professorsgatan 1, Lund. Date 12th Nov. 2021, at 9:15.

Faculty opponent
Prof. Bassam Dally, Mechanical Engineering
Physical Science and Engineering Division
King Abdullah University of Science and Technology, Saudi Arabia

Organization	Document name
LUND UNIVERSITY	DOCTORAL DISSERTATION
Division of Combustion Physics P.O.Box 118 SE-221 00 Lund, Sweden	**Date of issue** 2021-11-12
Author(s): Qingshuang Fan	Sponsoring organisation

Title and subtitle: Experimental investigation of premixed ammonia combustion at high Karlovitz number conditions

Abstract

This thesis aims to acquire deep knowledge on turbulent premixed combustion at high Karlovitz (Ka) number conditions with the help of laser-based diagnostic measurements.

Considering that ammonia (NH_3), as a carbon-free energy carrier, is a promising candidate for replacing conventional fossil fuels in the future, all the investigations in this work were carried out on ammonia/air premixed flames. Different optical diagnostic techniques, including planar laser-induced fluorescence (PLIF), laser Doppler anemometry (LDA) and Rayleigh scattering thermometry, have been employed for the measurement of key species, flow velocity and temperature, respectively.

Firstly, experimental research on ammonia/air premixed flames was conducted on the Lund University Pilot Jet burner (LUPJ). The flame structure was visualised through the simultaneous measurement of the temperature field together with NH radical distribution or with NO distribution. Five stoichiometric flames with Karlovitz (Ka) numbers ranging from 274 to 4720 were studied. The NH layer, used as a marker of fuel consumption layer, remains thin at the burner exit, but becomes progressively thickened along the flame height with increasing turbulent intensity (u'/S_L) when the Ka is higher than 1900. This thickness increase is attributed to the penetration of the small eddies and the merging of flame branches. The NO pollutant, mainly generated in the reaction zone, was observed to exist in a wide region, across the whole flame, because of the turbulent diffusivity and the flow convection.

Limited by the geometric scale, the turbulent Reynolds number (Re_t) in the LUPJ flame is much smaller than the operational ranges in industrial applications. For a better understanding of highly turbulent premixed combustion, a DRZ (distributed reaction zone) burner was introduced. This burner has integral scales (l_0) between 30 – 40 mm and wider working conditions with a maximum turbulent intensity (u'/S_L) and Karlovitz (Ka) number up to 240 and 1008. OH-/NH-PLIF and LDA measurements have been carried out to expand fundamental understanding. The results show that NH layer thickness remains almost constant and independent of turbulent intensity (u'/S_L), although all the cases are located in the distributed reaction zone regime (Ka > 100). The turbulent eddies can only wrinkle the flame surface instead of penetrating into the inner structures. The ratio of turbulent to laminar burning velocity (S_T/S_L) increases monotonously with the Karlovitz (Ka) number. All the signs indicate that the flamelet theory is still applicable for ammonia premixed combustion at high Karlovitz (Ka) number conditions, which is inconsistent with Peters' assumption in the Borghi-Peters diagram.

Key words: Turbulent premixed combustion; Ammonia flames; Laser diagnostics; Flame structure; High Karlovitz number; Turbulent burning velocity

Classification system and/or index terms (if any)

Supplementary bibliographical information		**Language** English
ISSN and key title 1102-8718		**ISBN** 978-91-8039-045-3 (print) 978-91-8039-046-0 (pdf)
Recipient's notes	**Number of pages** 85	Price
	Security classification	

Signature: 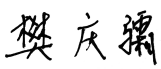 Date: 2021-10-04

Experimental investigation of premixed ammonia combustion at high Karlovitz number conditions

Qingshuang Fan

LUND
UNIVERSITY

Cover images by Qingshuang Fan and Xin Liu

Faculty of Engineering, Department of Physics
Division of Combustion Physics

Lund Reports on Combustion Physics: LRCP-238
ISBN 978-91-8039-045-3 (print)
ISBN 978-91-8039-046-0 (pdf)
ISSN 1102-8718
ISRN LUTFD2/TFCP-238-SE

Printed in Sweden by Media-Tryck, Lund University
Lund 2021

To my parents: thank you for your support, motivation, and inspiration.

To Xin and Chacha: thank you for your love and company.

"The job's not finished. Is the job finished? I don't think so."
2009/06/08

"Have you seen the look of Los Angeles at four o'clock in the morning?"
2012

"Somebody has to win, so why not be me?"
2013/08/23

"Those times when you get up early and you work hard, those times when you stay up late and you work hard, those times when you don't feel like working, you're too tired, you don't want to push yourself but you do it anyway: That is actually the dream. It's not the destination, it's the journey."

2017/12/18

Mamba Out
2020/01/26

Abstract

This thesis aims to acquire deep knowledge on turbulent premixed combustion at high Karlovitz (Ka) number conditions with the help of laser-based diagnostic measurements.

Considering that ammonia (NH_3), as a carbon-free energy carrier, is a promising candidate for replacing conventional fossil fuels in the future, all the investigations in this work were carried out on ammonia/air premixed flames. Different optical diagnostic techniques, including planar laser-induced fluorescence (PLIF), laser Doppler anemometry (LDA) and Rayleigh scattering thermometry, have been employed for the measurement of key species, flow velocity and temperature, respectively.

Firstly, experimental research on ammonia/air premixed flames was conducted on the Lund University Pilot Jet burner (LUPJ). The flame structure was visualised through the simultaneous measurement of the temperature field together with NH radical distribution or with NO distribution. Five stoichiometric flames with Karlovitz (Ka) numbers ranging from 274 to 4720 were studied. The NH layer, used as a marker of fuel consumption layer, remains thin at the burner exit, but becomes progressively thickened along the flame height with increasing turbulent intensity (u'/S_L) when the Ka is higher than 1900. This thickness increase is attributed to the penetration of the small eddies and the merging of flame branches. The NO pollutant, mainly generated in the reaction zone, was observed to exist in a wide region, across the whole flame, because of the turbulent diffusivity and the flow convection.

Limited by the geometric scale, the turbulent Reynolds number (Re_t) in the LUPJ flame is much smaller than the operational ranges in industrial applications. For a better understanding of highly turbulent premixed combustion, a DRZ (distributed reaction zone) burner was introduced. This burner has integral scales (l_0) between 30 – 40 mm and wider working conditions with a maximum turbulent intensity (u'/S_L) and Karlovitz (Ka) numbers up to 240 and 1008. OH-/NH-PLIF and LDA measurements have been carried out to expand fundamental understanding. The results show that NH layer thickness remains almost constant and independent of turbulent intensity (u'/S_L), although all the cases are located in the distributed reaction zone regime (Ka > 100). The turbulent eddies can only wrinkle the flame surface instead of penetrating into the inner structures. The ratio of turbulent to

laminar burning velocity (S_T/S_L) increases monotonously with the Karlovitz (Ka) number. All the signs indicate that the flamelet theory is still applicable for ammonia premixed combustion at high Karlovitz (Ka) number conditions, which is inconsistent with Peters' assumption in the Borghi-Peters diagram.

Popular science

The climate emergency has already become one of the biggest global issues and its effects will continue through the present century and beyond. Human and industrial activities related to burning fossil fuels (coal, oil, natural gas, etc.) are mainly responsible for the increase in greenhouse gas (GHG) emissions, leading to global climate change. To achieve the goal of large reductions in GHG emissions, the use of carbon-free fuels, instead of conventional fossil fuels, is one promising solution that has been proposed.

Ammonia (NH_3) is a colourless gas with a strong smell. Mainly used as fertiliser in agriculture, most ammonia is manufactured commercially through the Haber-Bosch process by combining nitrogen (N_2) and hydrogen (H_2). Recent research suggests the advantages of ammonia as a suitable energy carrier of renewable energy sources. Due to its carbon-free nature, green ammonia has also been regarded as a potential clean energy, like hydrogen, for future use in transportation, electricity, etc. Compared with traditional hydrocarbon fuels, utilisation of ammonia in combustion currently still faces different challenges although efforts have been made. The emission of nitrogen oxides (NO_x) during the burning process can be a critical problem in pure ammonia and ammonia-fuel blends. Ammonia's relatively low heat radiation, narrow flammability range, and high auto-ignition temperature have all limited its application in industrial fields. To overcome these problems, it is essential to gain a deeper understanding of the chemical and physical process of ammonia combustion.

Laser-based diagnostics is an effective method in experimental combustion research. Key parameters, including temperature, chemical species concentration, velocities, particle characteristics, etc., can be extracted from flames by employing advanced laser-based measurements. These techniques are non-intrusive, keeping the interrogation window undisturbed by any physical probes. Another advantage is that lasers can provide almost instantaneous results with high spatial and temporal resolutions, which is beneficial for the investigation especially in turbulent combustion, where the turbulent flow consists of eddies with different characteristics time scales, and some of the intermediate radicals are unstable and shot-lived. The technology can extend the point/line measurement to plane or even volume measurement, according to specific conditions and requirements. Simultaneous application of multiple laser techniques allows for multi-scalar information, giving insights to analyse their interaction and correlation.

Furthermore, the experimental data, with high accuracy, can improve the development and validation of combustion models in numerical simulations. Because of these merits, laser-based diagnostics have been regarded as a powerful tool to study various combustion phenomena.

In this thesis, two burners were selected for investigation. One is laboratorial with small geometry scale for fundamental studies, and the other is a Bunsen burner which can run at real gas turbine conditions, intended for industrial applications. Both burners adopt a pilot methane/air flame to stabilise the centre ammonia/air flame with a higher jet speed, preventing flame extinction from the entrainment of ambient air. Three laser diagnostics techniques were involved in this study. Laser Doppler anemometer (LDA) was used to measure the characteristic velocities and integral scales, to provide an overview of the turbulent intensity distribution. Different radicals generated from the combustion process were visualised by simultaneous planar laser-induced fluorescence (PLIF), which can help to explain the interaction between the turbulence and chemistry. Additionally, Rayleigh scattering thermometry was also employed as a complementary technique for temperature imaging in combustion environments. The aim of the research in this work is to help gain fundamental knowledge on ammonia premixed combustion at high Karlovitz (Ka) number conditions, as well as provide experimental data for combustion model validation and development. Moreover, with the observations and conclusions obtained from this thesis, some useful guidance can be provided regarding gas turbine combustor design related to ammonia fuels, in order to help to mitigate the world's energy shortage.

List of papers

I. **Q. S. Fan**, X. Liu, L. L. Xu, A. A. Subash, C. Brackmann, M. Aldén, X. S. Bai and Z. S. Li. Flame structure and burning velocity of ammonia/air turbulent premixed flames at high Karlovitz number conditions.
Manuscript submitted to Combustion and Flame, 2021.

II. **Q. S. Fan**, X. Liu, X. Cai, C. Brackmann, M. Aldén, X. S. Bai and Z. S. Li. Structure and scalar correlation of ammonia/air turbulent premixed flames in the distributed reaction zone regime.
Manuscript submitted to Combustion and Flame, 2021.

III. X. Cai, **Q. S. Fan**, X. Liu, C. Brackmann, W. Weng, J. Wang, Z. Huang, M. Aldén, X. S. Bai and Z. S. Li. Role of differential diffusion in the structure of premixed ammonia/hydrogen/air flames in the distributed reaction zone regime.
Manuscript submitted to Combustion and Flame, 2021.

Related work

A. J. L. Gao, **Q. S. Fan**, X. Liu, B. Li, E. Kristinsson, M. Aldén and Z. S. Li. Sensitive planar laser-induced imaging of CH and CH_3 for reaction-zone flame visualization in premixed methane/air flames over broad stoichiometric ratios.
Manuscript submitted to Combustion and Flame, 2021.

B. C. D. Kong, **Q. S. Fan**, X. Liu, A. A. Subash, T. Hurtig, A. Ehn, M. Aldén and Z. S. Li. Non-thermal gliding arc discharge assisted turbulent combustion (up to 80 kW) at extended conditions: phenomenological mechanism.
Manuscript submitted to Combustion and Flame, 2021.

C. X. Liu, A. A. Subash, **Q. S. Fan**, C. Brackmann, J. Evers, M. Aldén and Z. S. Li. Visualization of turbulent inverse diffusion flames at elevated pressure using OH-PLIF and OH^* chemiluminescence imaging.
In Proceedings of the 9th European Combustion Meeting, 2019.

D. L. L. Xu, F. Pignatelli, **Q. S. Fan**, X. Cai, X. S. Bai, Z. S. Li and M. Aldén. Large eddy simulation of turbulent premixed ammonia jet flames at high Karlovitz number conditions.
Manuscript to be submitted.

E. L. L. Xu, F. Pignatelli, **Q. S. Fan**, X. Liu, X. S. Bai, Z. S. Li and M. Aldén. Experimental and numerical study of the flame structure of ammonia/air premixed flames at extreme turbulence conditions.
Manuscript to be submitted.

Abbreviations

DNS	Direct Numerical Simulation
DRZ	Distributed Reaction Zone
FFT	Fast Fourier Transform
FSD	Flame Surface Density
FWHM	Full Width at Half Maximum
GHG	Greenhouse Gas
HRR	Heat release rate
ICCD	Intensified Charge-coupled Device
LDA	Laser Doppler Anemometry
LUPJ	Lund University Piloted Jet burner
Nd: YAG	Neodymium-doped Yttrium Aluminium Garnet
PDF	Probability density functions
PDS	Power Density Spectrum
PIV	Particle Image Velocimetry
PLIF	Planar Laser-induced Fluorescence
RMS	Root Mean Square
TRZ	Thin Reaction Zone
UHC	Unburned Hydrocarbon

Nomenclature

$\langle A \rangle$	Mean flame brush area
$\langle C \rangle$	Mean progress variable
D	Thermal diffusivity
Da	Damköhler number
D_T	Turbulent diffusivity of mass
f	Focus length
I	Turbulence velocity
I	Intensity of incident light
k	Boltzmann's constant
Ka	Karlovitz number
l_0	Integral length scale
$\dot{m}$	Mass flow rate
N	Number density
P	Pressure
Re_t	Turbulent Reynolds number
Sc	Schmidt number
S_L	Laminar flame speed
S_T	Turbulent burning velocity
T	Temperature
T_p	Temperature of products
T_u	Temperature of reactants
τ_{chem}	Effective chemical time
τ_F	Flame time
u'	Turbulent velocity
U	Mean velocity
μ	Dynamic viscosity
η	Kolmogorov scale
Φ	Equivalent ratio
λ	Wavelength
θ	Angle between the beams
$\delta_{L,NH}$	NH layer thickness
δ_L	Laminar flame thickness
Σ	Flame surface density
ρ	Density
ε	Dissipation rate
ν	Kinematic viscosity

Table of Contents

1 Introduction

1.1 Motivations

Combustion has played an important role in the development of human history. From the early days, when human beings utilised fire to survive, up to the modern understanding of the burning process, combustion phenomena can be regarded as a vital force to promote the progress of human civilisation. More importantly, the development of combustion technology enables energy to be converted into heat and power through the combustion process. Combustion technology has been widely used in various fields, including electric power generation, transportation, and the aviation industry. However, most power generation systems still use fossil fuels (coal, oil, natural gas, etc.) and this reliance is unlikely to decline in the foreseeable future, which may lead to a serious global energy crisis [1].

Formed from the carbon-rich remains of dead animals and plants over millions of years, fossil fuels are non-renewable, and we have a limited supply. In addition, climate change, mainly caused by greenhouse gas (GHG) emissions from fossil fuel utilisation, has also attracted widespread public attention. Although the largest-ever decrease in global emissions was seen in 2020, due to the COVID-19 pandemic, monthly data show a rapid rebound of carbon dioxide (CO_2) emissions through the rest of the year [2]. Moreover, combustion products contain several air pollutants, like carbon monoxide (CO), nitrogen oxides (NO_x), soot or unburned hydrocarbons (UHC), which are harmful to the global environment and human health. Therefore, it is urgent to find other alternative and renewable energy sources.

Since the combustion product is only water (H_2O), hydrogen (H_2) has been regarded as a clean fuel for the next decade. Advantages including its large scale production and higher gravimetric energy density make the hydrogen economy a bright future prospect [3]. However, problems related to hydrogen's storage, transportation, and low volumetric energy density, have prompted people to look for other alternative fuels or energy carriers. Ammonia (NH_3), as a promising candidate, has gained a lot of attention recently. Ammonia is one of the carbon-free fuels and safe hydrogen-carrier with low reactivities. It can also be manufactured in different ways [4, 5]. A recent study has discovered a new, environmentally friendly process to overcome the carbon-intensive problem, which is the main issue in the Haber-Bosch process [6]. In addition, the storage

and transport of the ammonia can be made more efficient, with lower costs compared to hydrogen [7]. Nevertheless, some drawbacks hinder the industrial application of ammonia combustion, including low combustion intensity (combustion heat and laminar burning speed), large amounts of NO_x emission, etc. Therefore, investigation of ammonia flames to overcome these challenges has attracted much interest.

Turbulent premixed combustion is widely used in various types of combustors, e.g., stationary gas turbines and spark-ignition (SI) engines. It is a complicated process involving non-linear and multi-scale interactions between the turbulence and chemistry. The flame characteristics are altered by the intense mixing and enhanced transport. Meanwhile, the thermochemistry also has an influence on the turbulence through thermal expansion. However, one can control the flame temperature to reduce the thermal NO_x formation by adjusting the equivalence ratio (Φ) of reactants. Because of its relatively low laminar burning speed (S_L) and large laminar flame thickness (δ_L), compared to hydrocarbon flames, ammonia/air premixed combustion in practical devices can easily achieve high turbulent intensity (u'/S_L). Experimental studies on ammonia premixed combustion under highly turbulent conditions can provide more information for in-depth understanding of the turbulence/flame interaction. Since the combustion model should be based on physical principles and reliable experimental observation instead of intuition and empiricism [8], results and knowledge from the experimental studies also play an important role in numerical simulation, and will be valuable for the design of future combustors.

Current studies of premixed ammonia/air combustion are on the low or moderate turbulent levels [9, 10]. Comparatively limited research was conducted at highly turbulent intensities similar to those of industrial gas turbine engine operating conditions [11-13], and visualisation and characterisation of flame structure by means of advanced non-intrusive laser diagnostic techniques are especially lacking. This thesis presents laser-based diagnostic measurements of fundamental flame properties of premixed ammonia/air combustion under high Karlovitz (Ka) number conditions. The work aims to gain deeper knowledge of the physics and chemistry in ammonia flames operated in the distributed reaction zones (DRZ) regime.

1.2 Outline

The content of this doctoral dissertation consists of five chapters:

Chapter 1: This chapter gives a brief background relevant to the research and indicates the research purpose of this thesis.

Chapter 2: A short review of the properties of laminar premixed flame is provided. The Borghi-Peters diagram is then used to classify the turbulent premixed flames into different regimes, and the theory of turbulent burning velocity is demonstrated considering the effects of flame wrinkling and turbulent diffusivities. Finally, summaries of related work motivating this dissertation are discussed.

Chapter 3: The purpose of this chapter is to illustrate the burners and laser-based diagnostic methods involved in this thesis. Two burners are employed, one in laboratory-scale used for fundamental studies, and another with a large geometric structure with flame power equal to that of industrial combustors. The basic principles of different laser diagnostic techniques are described in detail, including planar laser-induced fluorescence (PLIF), laser Doppler anemometry (LDA), and Rayleigh scattering thermometry.

Chapter 4: In Chapter 4, the image processing schemes are described that are used to extract the meaningful information from the raw images. Results are presented from the simultaneous optical measurement of the two flame structures on two burners, including the NH layer thickness, relationship between the turbulence and chemical reactions, turbulent burning velocity, etc. All of the selected cases are located in the regime of distributed reaction zones (DRZ) in the Borghi-Peters diagram.

Chapter 5: Based on the results from the experimental investigations throughout this work, conclusions are drawn at the end of the thesis, and suggestions regarding future work are given. This doctoral dissertation takes the first step to gain fundamental knowledge on premixed ammonia/air combustion at high Karlovitz number, although many problems remain to be solved.

2 Turbulent premixed combustion at high Karlovitz number conditions

The structure of the laminar ammonia/air premixed flame is briefly introduced. The features of turbulent flow and Borghi-Peters diagram are discussed next, followed by a theoretical analysis of turbulent burning velocity. Research progress regarding the distributed reaction zone is given at the end of the chapter.

2.1 Laminar premixed flames

Before discussing the features of turbulent premixed combustion, the properties of laminar premixed flames should be reviewed. Based on a chemical reduced mechanism [14], an overall structure of NH_3/air stoichiometric flames is shown in Fig. 2.1.

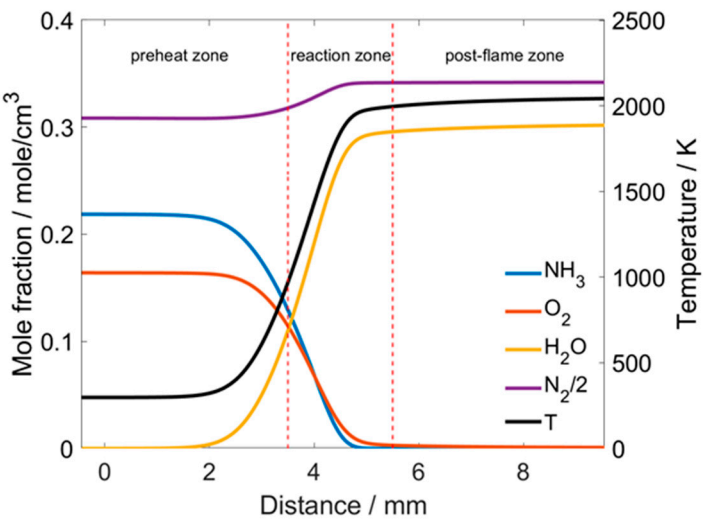

Fig. 2.1. An overall structure of NH_3/air stoichiometric flames at P = 0.1 MPa.

Similar to the CH_4/air flames, the structures of NH_3/air flames can be represented by a three-zone model: the preheat zone, where the reactants are continuously

heated by the combustion products downstream through diffusion; the reaction zone, where ammonia and oxygen are consumed and combustion intermediates (i.e., H_2) are formed with major heat release; and the post-flame zone, in which reactions have reached equilibrium and final products, including H_2O and N_2, are formed. Since the reaction zone is the main region where most reactions occur, studies of this zone have particular importance. Fig. 2.2 shows the profiles of key species and heat release rate (HRR) in this thin region. In view of flame chemistry, ammonia first decomposes to NH_i (i = 0, 1, 2) with reactive radicals including OH, H, and O. The intermediates NH_i are consumed, resulting in the formation of NO and N_2 based on the amount of O/H in the radical pool [4]. It can be seen that profiles of several species correlate well with HRR distribution and some of the radicals even locate inside the HRR region, with the potential to be markers of the flame front. In view of internal structure, the reaction zone can still be divided into two layers: a fuel consumption layer and an oxidation layer, considering the degree of reaction rate. The fuel consumption layer is also referred to as the inner layer of a premixed flame [15], whose thickness is assumed to be approximately one tenth of the methane flame thickness [8]. In ammonia flames, the fuel consumption layer (inner layer) is the overlapping layer of NH_3 and OH, which coincides with the NH profile. Thus, NH radical can be used to indicate the location and thickness of the fuel consumption layer of the ammonia/air flames. A recent publication also indicated that NH-PLIF signals can be taken to indicate the inner reaction layer where ammonia is consumed [16]. The oxidation layer is the overlap of H_2 and OH, which is much thicker than the inner layer.

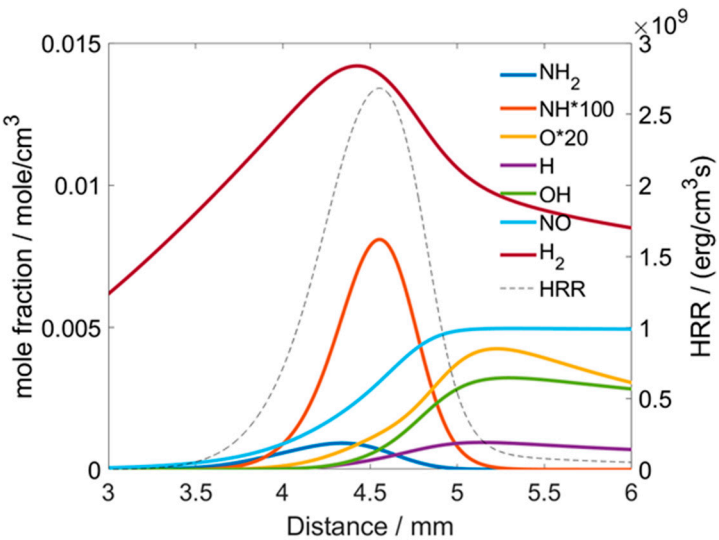

Fig. 2.2. Profiles of mole fraction of key species and heat release rate (HRR) in reaction zone.

Two intrinsic parameters to characterise laminar premixed flames are laminar flame speed (S_L) and laminar flame thickness (δ_L), which will be used to normalise the turbulent quantities in Section 2.2. The value of S_L varies between 2 to 8 cm/s with different equivalence ratios, and this flame propagation speed is much smaller than that of corresponding hydrocarbon flames. The δ_L is generally defined as the sum of the thickness of the preheat zone and fuel consumption layer [17]. However, this definition is not easy to achieve in real cases. A more convenient expression is defined as $\delta_L = (T_p - T_u)/|\nabla T|_{max}$, where T_p is the temperature of the products, T_u is the temperature of the reactants, and the denominator is the maximum temperature gradient. This expression will be employed in this thesis to quantify the flame thickness [18]. These two parameters can be connected with each other, following the work of Zel'dovich et al. [19]:

$$S_L \sim \sqrt{D/\tau_{chem}} \quad \delta_L \sim \sqrt{D\tau_{chem}} \tag{2.1}$$

where D is the thermal diffusivity and τ_{chem} is the effective chemical time related to the reaction rate and reactant density. Then the flame time τ_F, indicating the time that the premixed flame front propagates through a distance equal to the flame thickness, can be written macroscopically as the ratio of flame thickness to flame speed, which is proportional to the effective chemical time.

$$\tau_F = \frac{\delta_L}{S_L} \sim \tau_{chem} \tag{2.2}$$

2.2 Turbulent flows and the Borghi-Peters diagram

As the last great unsolved problem of classical physics, turbulent flows are prevalent in nature and industrial applications. Sutton (1955) defined turbulence as: "a state of fluid flow in which the instantaneous velocities exhibit irregular and apparently random fluctuations" [20]. Although this definition is incomplete and not precise, the statement reviews two characteristics to describe the turbulence. Apart from these, enhancement of transport of mass, momentum and heat, dissipation, and other key features are concluded after further exploration [21]. Richardson (1922) proposed that the turbulence consists of eddies with a wide range of characteristic scales. Large eddies are unstable and will break up into smaller eddies, transferring energies to them. This process, called energy cascade, goes on successively and ends up in dissipation by viscosity, as shown in Fig. 2.3, which can be summarised as "Big whirls have little whirls that feed on their velocity, and little whirls have lesser whorls and so on to viscosity …… in the molecular sense" [22]. The description can also be expressed mathematically in a more intuitive way by equation (2.3).

$$u'(x) = \sum_{1}^{N} a_n \sin(k_n x + \varphi_n) \tag{2.3}$$

Turbulent velocity (u') (defined as the root-mean-square (rms) of the velocity fluctuations) along the distance (x) can be written as the sum of n numbers of sine waves according to Fourier series. a_n and φ_n are the Fourier coefficient. k_n is the wavenumber and connected to characteristic length scales (l_n) in turbulence by $k_n = 2\pi/l_n$.

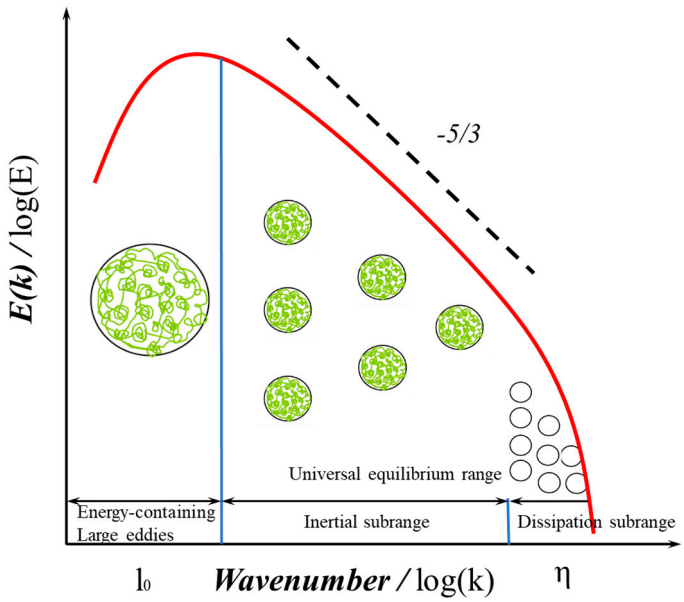

Fig. 2.3. Schematic of energy cascade progress and the distribution of turbulent kinetic energy spectrum.

The energy cascade can be divided into three major regions based on the Kolmogorov hypotheses [23] and two characteristic length scales: integral scales l_0 and Kolmogorov scales η, illustrated in Fig. 2.3. The energy-containing range involves large scales of turbulence, in which the main turbulent kinetic energy generated at length scales in the order of integral scales l_0. Small eddies are all located in universal equilibrium range, whose motions are statistically isotropic and have a universal form determined by dissipation rate ε and kinematic viscosity ν. This range can further be separated into two subranges: the inertial subrange and the dissipation subrange. In the dissipation subrange, eddies having the same magnitude of the Kolmogorov scales η (represented as the very smallest, dissipative eddies) are dissipated rapidly into heat as viscous effects are in the dominant position. Between the energy-containing and dissipation subrange is the

inertial subrange, where the energies are transferred with a rate nearly equal to the dissipation rate ε and the viscous effects can be ignored [24]. Useful equations are derived by using dimensional analysis using the above hypotheses:

$$Re_{\mathrm{t}} = \frac{u'\mathrm{l}_0}{\nu} \tag{2.4}$$

$$\eta = (\nu^3/\varepsilon)^{1/4} \qquad u_\eta = (\varepsilon\nu)^{1/4} \qquad \tau_\eta = (\nu/\varepsilon)^{1/2} \tag{2.5}$$

$$\eta/\mathrm{l}_0 \sim Re_t^{-3/4} \qquad u_\eta/u_0 \sim Re_{\mathrm{t}}^{-1/4} \qquad \tau_\eta/\tau_0 \sim Re_{\mathrm{t}}^{-1/2} \tag{2.6}$$

Where Re_t is the turbulent Reynolds number, and u_η and τ_η are the Kolmogorov velocity scales and residence time scales.

Turbulent premixed combustion has been applied in many engineering fields. However, turbulence strongly interacts with the chemistry process in turbulent flow, and the heat release from combustion will change the flow properties in turns affecting the flow field. To simplify the complication in turbulent premixed combustion, and quantify the correlation of the turbulence/chemistry, Borghi [25, 26] proposed a diagram using theoretical scaling analysis to separate the turbulent premixed flames into different regimes. The most common version is refined and modified by Peters [8], presented in Fig. 2.4.

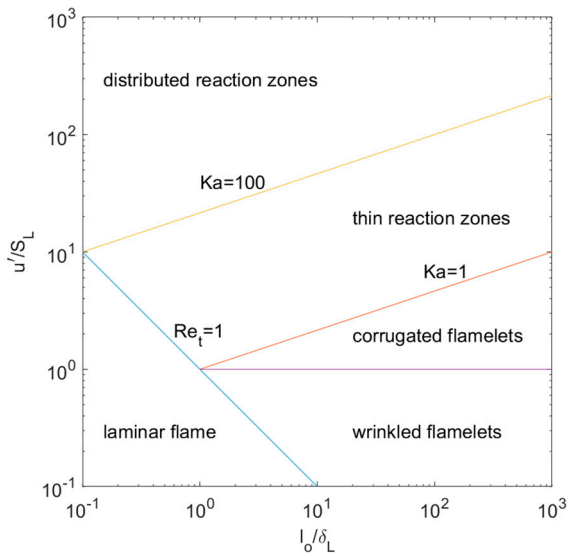

Fig. 2.4. Borghi-Peters regime diagram for turbulent premixed combustion.

Before discussing the above diagram, two more non-dimensional parameters are introduced, based on the turbulence and laminar flame properties and usually used as classified criteria. The Damköhler number (Da) is defined as the ratio of the residence time of large eddies to the flame time τ_F. The Karlovitz number (Ka) is the ratio between the flame time τ_F and the residence time of Kolmogorov eddies. These two numbers can be correlated by turbulent Reynolds number (Re_t) with the assumption that the Schmidt number (Sc) is unity.

$$Re_t = \frac{u' \mathrm{l}_0}{\nu} \sim \frac{u' \mathrm{l}_0}{\mathrm{S}_L \delta_L} \tag{2.7}$$

$$Da = \frac{\tau_0}{\tau_F} = \frac{\mathrm{l}_0 \mathrm{S}_L}{u' \delta_L} \tag{2.8}$$

$$Ka = \frac{\tau_F}{\tau_\eta} = \frac{\delta_L u_\eta}{\mathrm{S}_L \eta} \sim \left(\frac{\delta_L}{\eta}\right)^2 \tag{2.9}$$

Five regimes are seen in the Borghi-Peters diagram according to the normalised integral scale (l_0/δ_L) against the turbulent intensity ($u'/\mathrm{S_L}$). The flow is laminar when $Re_t < 1$. When the turbulent intensity is low at $Ka < 1$, all length scales are larger than the laminar flame thickness. The entire flame structure is embedded in Kolmogorov eddies. The turbulence can only wrinkle the flame front layer. The instantaneous turbulent flame shows a thin quasi-laminar flamelet front, which is not perturbed by turbulent velocity. As the turbulent intensity increases ($u' > \mathrm{S_L}$), pockets of reactants and products appear due to the merging of the instantaneous flame front induced by large-scale interactions.

In the regime of thin reaction zones (TRZ, $1 < Ka < 100$), the Kolmogorov length scale becomes smaller than the flame thickness, while remaining larger than the inner layer thickness, which is approximately one tenth of the flame thickness in methane/air premixed flames [15]. The turbulent effects on the flame fronts are more complicated, as the smallest eddies can pass through the flame, causing the preheat zone to broaden. However, fuel consumption will remain thin and intact. Experimental results [27-31] and numerical simulations [32-34] have already proved this theoretical hypothesis.

If $Ka > 100$, the Kolmogorov eddies have the possibility to penetrate the inner layer and the entire flame structure might be modified according to the theoretical analysis. The chemistry process can be disrupted locally because of enhanced heat loss upstream followed by the decrease in temperature and the loss of radicals [8]. The flame cannot sustain itself anymore, and local quenching will cause the flame to finally extinguish under this condition. On the other hand, chemical reactions

controlling the heat release may proceed and distribute across the whole combustion zone, owing to the enhancement of heat and mass transport. In this case, the concept of the flamelet is no longer applicable here. As few investigations have been conducted in this regime, it still remains unclear whether the regime of distributed reaction zone (DRZ) exists.

2.3 Turbulent burning velocity

Due to the effect of turbulence, mentioned above, the propagation speed of the turbulent flame front is altered compared with the laminar case. Two definitions of fuel consumption speed, often used to define the turbulent burning velocity (S_T), will be introduced.

The global consumption speed is the propagation speed of the mean flame surface towards the reactants [35, 36]:

$$S_{T,GC} = \frac{\dot{m}}{\rho_u \langle A \rangle} \tag{2.10}$$

where $\dot{m}$ is the mass flow rate of the reactants, ρ_u is the density of the unburnt mixture and $\langle A \rangle$ is the area of the ensemble-averaged mean flame surface. $\langle A \rangle$ is commonly defined using the iso-contour lines of the ensemble-averaged mean progress variable $\langle C \rangle$ based on OH radicals. The results can vary greatly depending on the selected value of $\langle C \rangle$ [9, 35, 37, 38]. This expression demonstrates how fast the product is formed, and it is beneficial for purposes of engineering and design.

The local consumption speed is based on the Damköhler prediction in the large-scale turbulence (low turbulent intensity) regime [39], in which the local flame will behave like a laminar flamelet [40, 41]:

$$S_{T,LC} = S_L I_0 \int_{-\infty}^{+\infty} \Sigma dx_n \tag{2.11}$$

where I_0 is the stretch factor, Σ is the flame surface density (FSD) and x_n is the spatial coordinate along the normal direction of the mean flame surface. This definition is usually used in combination with equation (2.10) to analyse the effect of flame surface density variation on the turbulent burning velocity.

Damköhler [39] tried to obtain the turbulent burning velocity from the early experimental data. He suggested that the turbulent burning velocity only depends on wrinkled instantaneous flame front area (A_T) in the flamelet regime, and increases linearly with the turbulent intensity:

$$\frac{S_T}{S_L} = \frac{A_T}{A_L} = 1 + \frac{u'}{S_L} \tag{2.12}$$

For high-intensity, small-scale turbulence, Damköhler assumed that turbulence will modify the transport properties with an enhanced eddy diffusivity to replace the molecular diffusivity, because eddies can pass through the flame, as mentioned in the previous section. Compared with the laminar case, as depicted in equation (2.1), the turbulent burning velocity is illustrated as:

$$\frac{S_T}{S_L} \sim \sqrt{\frac{D_T}{D}} \sim \sqrt{\frac{u' l_0}{\nu}} = Re_t^{1/2} \tag{2.13}$$

where D_T is the turbulent diffusivity of mass, which is proportional to the product of turbulent velocity and integral length scale. This model shows a slow increase of the turbulent burning velocity at intermediate turbulent intensity. When the turbulent intensity further increases, the two assumptions are invalid. Better relations to correlate significant parameters, including turbulent diffusivity, increased reaction rate, turbulent intensity, etc. remain to be investigated.

2.4 Distributed reaction zones regime

Experimental research on premixed flames under high Karlovitz number conditions has been reported recently for hydrocarbon flames [27, 28, 42-50]. Questions related to how premixed flames behave at extreme levels of turbulence, and the characteristics of distributed reaction zones in the regime diagram of Borghi-Peters in Fig. 2.4, remain unresolved.

The structure of methane/air flames exhibits a significant change in the reaction zone with an increasing Karlovitz number. When Ka is between 10 and 100, Zhou et al. [43-45] found that the heat release layer (marked by HCO radicals or the overlapping region of formaldehyde (CH_2O) and hydroxyl (OH) radicals) and the inner layer (marked by CH radicals) were thin, similarly to the thickness of laminar flames, while the preheat zone (marked by the CH_2O layer) gradually broadened with increase in Ka. When the Karlovitz number is greater than 100, the CH layer, the HCO layer, and the overlapping layer of OH and CH_2O were all clearly observed to broaden, experimentally confirming the existence of the DRZ. Also, the Rayleigh scattering results from Zhou et al. [43-45] showed that the temperature gradient across the flame reduced as the flame broadened and Dunn et al. [42, 49, 50] drew similar conclusions from their measurements.

By using a similar measurement (CH-PLIF and overlapping region of CH_2O- and OH-PLIF) on methane/air flames in a Hi-Pilot burner, Driscoll et al. [28, 46-48] showed that the average thickness of the reaction layer remained almost constant

even when Ka is so high as 533, and the turbulence level (u'/S_L) is 246, and subsequently a new criterion to delimit regimes based on their measurements, combined with previous experimental studies and numerical simulations, was proposed. The different observations of the flame structure at high Karlovitz numbers are mainly due to differences in the burner geometric configurations, i.e., the integral length scale of the flames and the different excitation-detection strategies.

Recently, Mohammadnejad et al. [51] conducted simultaneous PLIF measurement of CH_2O and OH radicals in the lean methane/air flames using a Bunsen burner with a large diameter, similar to that of Driscoll et al. [28, 46-48]. They observed that the thickness of the preheat and heat-release layer became thicker by a factor of 6.2 and 3.9 compared to that of the corresponding laminar flames separately when the Karlovitz number was 76. Their findings are in agreement with the results of Zhou et al. [43-45] but at a lower Karlovitz number. The analysis based on stereoscopic particle image velocimetry (PIV) results suggested that the eddies with enough turbulent kinetic energy are able to penetrate into the reaction zone, which is consistent with Peters' assumption. However, this conclusion is inconsistent with the report from Driscoll et al. [52], that the integral length scales increased through the preheat zone because small-scale eddies are all dissipated in this layer.

Results from a series of direct numerical simulations (DNS) studies have also proven the existence of distributed reaction zones. Aspden et al. [53] showed that distributed burning appeared in hydrogen/air flames when the Karlovitz number is 8767, and the thickness of the reaction layer can be fifteen times that in a laminar flame. Lapointe et al. [54] observed the broadening reaction zone locally as the enhanced turbulent diffusivities. Wang et al. [55] performed DNS to reproduce the work of Zhou et al. [43-45]. The results of the flame surface density (FSD) and curvature correlated well with the experimental data. Spatial broadened distribution of the heat release surrogate can be recognised at the flame tip.

3 Burners and optical measurements

In this chapter, a brief description of the burners involved in this work is provided. The principle and methods of laser-based diagnostics, including planar laser-induced fluorescence, laser Doppler anemometry and Rayleigh scattering thermometry, are also presented.

3.1 Burners

3.1.1 **LUPJ burner**

The Lund University Piloted Jet (LUPJ) burner is a modified Mckenna-type burner used to produce highly turbulent premixed flames on laboratory scales. This burner consists of a centre nozzle with a diameter of 1.5 mm to generate an ammonia/air premixed jet flame. A methane/air premixed pilot flame, which is burned on the 61 mm diameter porous plug burner, provides a high-temperature environment to stabilise the inner high-speed jet flame by preventing the entrainment of outer ambient air. A more detailed description of the LUPJ burner can be found in Refs. [44, 56]. Photographs of chemiluminescence from ammonia/air premixed flames under laminar and turbulent conditions are shown in Fig. 3.1. A continuous flame front with a cone shape can be observed in the laminar flame, whereas the turbulent flame has a wider flame brush. The yellow colour can be attributed to the chemiluminescence from NH_2 [57, 58]. Experimental work related to a series of PLIF and Rayleigh scattering measurements were conducted on this burner, which will be presented in Section 4.1.

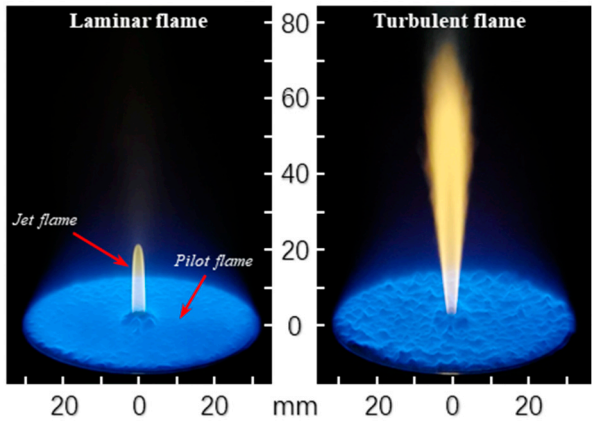

Fig. 3.1. Photographs of typical NH_3/air jet premixed flames on LUPJ burner.

3.1.2 **DRZ burner**

A burner made of stainless steel, aimed at investigating turbulent premixed flames in the distributed reaction zone regime, called the DRZ burner, was designed in this thesis work. A schematic of the burner, with auxiliary elements and a photograph of the actual burner and a premixed turbulent ammonia/air flame on it, is shown in Fig. 3.2.

This burner has a configuration similar to the Michigan Hi-Pilot burner [59] and it can also be regarded as an enlarged version of the LUPJ burner, mentioned above in section 3.1.1. The burner can be divided into two parts, the nozzle section and the co-flow chamber, used to generate the jet flame and pilot flame separately. The exit diameter of the jet nozzle is 22 mm, and it is located 20 mm above the titanium porous plug of the pilot flame burner, which has a diameter of 110 mm. For the jet flow, the ambient air is supplied by two blowers mounted in the atmospheric pressure test rig at Lund University [60], which has the capability to provide an airflow of approximately 50 g/s with a temperature adjustable from 300 ~ 650 K. The ammonia is introduced into the plenum chamber by eight separate inlets (7), mixing with the incoming airflow in a cylinder of glass beads (6) with a diameter of 6 mm and uniform by a perforated plate (5). The reactants then go through a turbulent generator (3) to increase the turbulent intensity and pass by a converging-diverging nozzle, exiting with a high speed and intense turbulence. The structure of the nozzle can prevent flashback of the flame because the velocity decreases when the mixture expands at the diverging section. For the co-flow part, air and methane will be premixed before being injected into the co-flow chamber and the mixture will go through the titanium porous plug plate (1) via eight other

inlets (2), forming hot co-flow gas to stabilise the centre jet. The other two inlets (4) are used as the tracer particle inlet for LDA/PIV measurements.

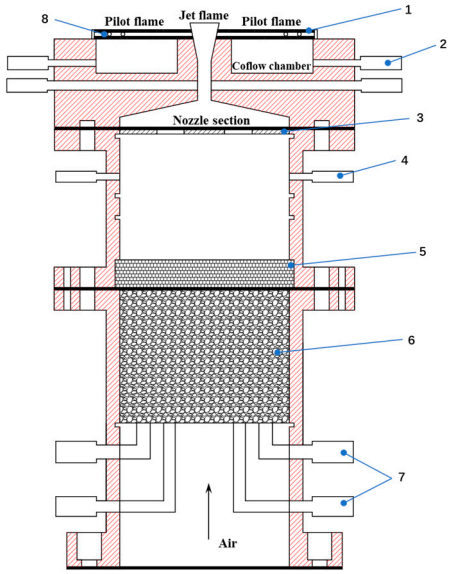

1.	Porous plug plate
2.	Inlets of coflow
3.	Turbulent generator plate
4.	Inlets of powder particles
5.	Perforated plate
6.	Glass ball
7.	Inlets of ammonia
8.	Water pipe

(a)

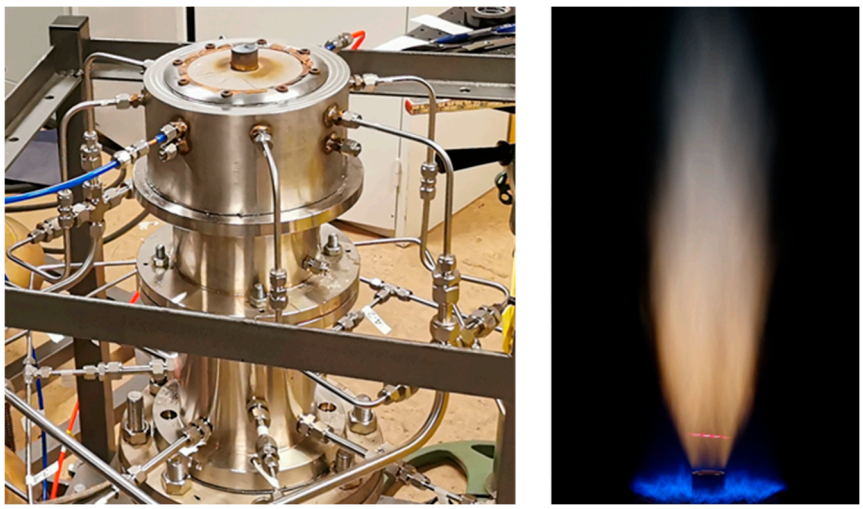

(b)

Fig. 3.2. (a) Schematic of the DRZ burner, (b) images of the actual burner and a premixed turbulent ammonia/air flame.

3.2 Laser-based diagnostic techniques

3.2.1 **Planar laser-induced fluorescence**

Planar laser-induced fluorescence (PLIF) as an optical technique is widely used in flames for species detection [61, 62], especially in studies of turbulent combustion. The concentration of radicals and pollutants can be detected at the level of ppm as well as sub-ppm. Great efforts have been made to extend this technique from qualitative to quantitative, that is from planar to volume measurement [63, 64].

A schematic of the typical transition for a diatomic molecule in two electronic states, provided in Fig. 3.3, is used to depict the laser-induced fluorescence process. The species of interest is excited from the ground state (X) to an excited state (A) by a specific laser wavelength. The excited species is unstable and will return to the ground state (X) with spontaneous fluorescence emission within nanoseconds to microseconds. Due to energy redistribution after the excitation, the fluorescence wavelength can be different from that of the excitation laser light, and is primarily shifted towards longer wavelengths, which avoid the interferences from elastic scattering.

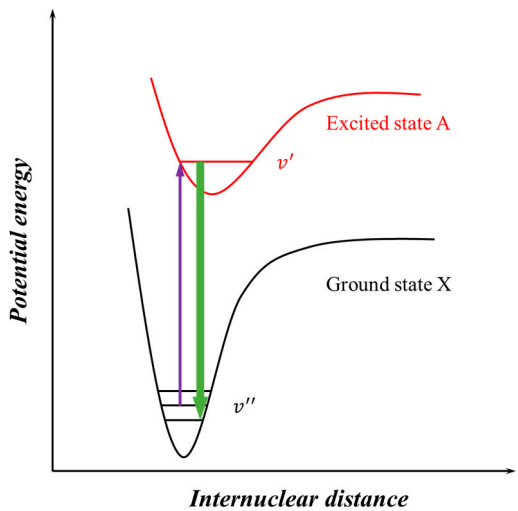

Fig. 3.3. Schematic of the laser-induced fluorescence process between two electronic states.

The fluorescence signal can be converted to species concentration, indicating spatial distribution of the selected species. For example, when the laser power is

lower than the saturation irradiance, the PLIF signal F is in the linear regime and can be expressed as [61]:

$$F = \frac{h\nu}{c}\frac{\Omega}{4\pi}VN_1^0B_{12}I\frac{A_{21}}{A_{21}+Q_{21}} \tag{3.1}$$

where $h\nu$ is the emitted photon energy, c is the speed of light, Ω is the collection solid angle, V is the detection volume, N_1^0 is the species population in the ground state before laser excitation, B_{12} is the Einstein coefficient for absorption, I is the intensity of incident light, A_{21} is the rate constant for spontaneous emission, and Q_{21} is the collisional quenching rate constant.

PLIF measurements were performed to visualise the turbulent flame structure in the thesis, and the information extracted from the local flame structure will be given in Chapter 4. Three key species involved in turbulent ammonia combustion are measured and the excitation-detection strategies for each are summarised in Table 3.1.

Table 3.1. Strategies of PLIF measurements for the species in this work

Species	Excitation wavelength	Detection wavelength	Filter
NH	~ 303.6 nm	~ 336 nm	WG335
OH	~ 283.5 nm	~ 309 nm	320 ± 20 nm
NO	~ 225.5 nm	230 ~ 400 nm	

3.2.2 Laser Doppler anemometry

Laser Doppler anemometry (LDA) is a widely accepted tool for the investigation of fluid dynamics. It has particular advantages in being non-intrusive, having high spatiotemporal resolution, and being calibration free. In this thesis, the turbulent quantities were measured by a two-component LDA system (FlowExplorer 2D High Power Optics, Dantec Dynamics). A typical schematic of the whole system is shown in Fig. 3.4. Two laser beams at different wavelengths (660/785 nm) were passed through the transmitting optics and focused in the probe volume. Fringes will be generated in this ellipsoidal volume as a result of interference phenomenon. The distance between neighbouring fringes can be expressed as the following:

$$d_f = \frac{\lambda}{2\sin\frac{\theta}{2}} \tag{3.2}$$

where d_f is the fringe distance, λ is the wavelength of the incident light, and θ is the angle between the beams.

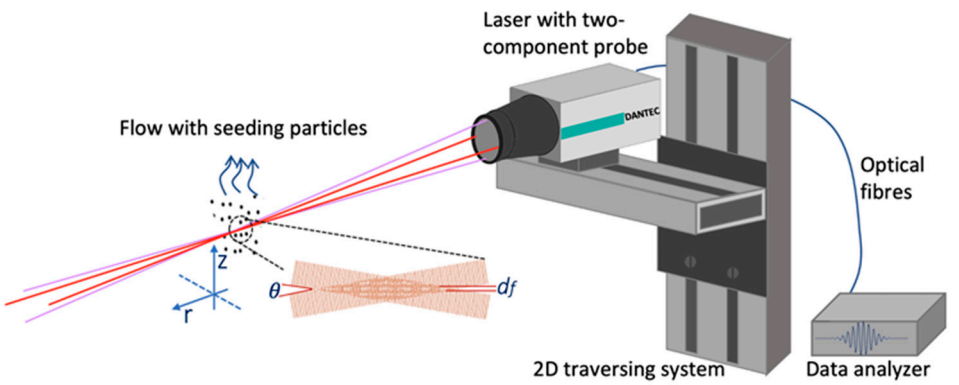

Fig. 3.4. Schematic of a 2D LDA system. The figure is taken from [65].

When a particle crosses over the fringe pattern, the signal of scattered light is collected backward by receiving optics. The difference between the incident light and scattered light is called Doppler shift (f_d) due to the Doppler effect, which is only proportional to the velocity projection perpendicular to the fringes and the laser wavelength. The velocity (v) can be calculated by:

$$\mathrm{v} = f_d \times d_f \tag{3.3}$$

One issue that needs to be considered in LDA measurement is direction ambiguity, because the same detected signal would be obtained if the flow direction were totally reversed. To overcome this problem, the Bragg cell included in the transmitting optics was used to split the laser into two beams of equal intensity, with one of the beams frequency-shifted (f_{shift}). The flow direction can be recognised as positive, negative, or zero, according to this shifted frequency.

The converted Doppler signals are filtered and amplified by a burst spectrum analyser (BSA F800-2D processor, Dantec Dynamics). Commercial software BSA Flow is used to carry out further processing, including moments, correlation, and spectrum. More details on the post-process will be described in section 4.3.1.

3.2.3 **Rayleigh scattering thermometry**

Rayleigh scattering thermometry is a straightforward way to acquire temperature distribution in flames. The intensity of Rayleigh scattering (I_s) depends on the total number density of molecules in a gas mixture:

$$I_s = IN\sigma_{mix}C \tag{3.4}$$

Where I is the intensity of incident light, N is the number density, σ_{mix} is the effective Rayleigh scattering cross section, and C is a constant related to solid angle, length of probe volume, and collection efficiency.

The gas temperature (T) is inversely proportional to this number density according to the ideal gas law:

$$P = NkT \tag{3.5}$$

Where k is the Boltzmann's constant and P is the pressure.

Before the measurement, calibration is needed to determine the reference parameters (I_{ref}, σ_{ref}, and T_{ref}) under known conditions, usually using pure nitrogen at room temperature. If the pressure (P) is uniform in the flow and the effective Rayleigh scattering cross section is known, then the flame temperature can be written in equation (3.6) by combining equations (3.4) and (3.5).

$$T = T_{ref} \frac{I_{ref}}{I} \frac{\sigma_{mix}}{\sigma_{ref}} \tag{3.6}$$

The main species in ammonia/air premixed flames and their Rayleigh scattering cross sections are shown in Table 3.2. All the cross sections are taken from Refs. [66, 67] except the ammonia gas, whose cross section is 1.6 times that of nitrogen, which was measured on the LUPJ burner. The detailed procedures of temperature conversion will be given in section 4.1.2.

Table 3.2. Rayleigh scattering cross sections of different species in ammonia/air flames at the 532 nm wavelength

Molecule	**N_2**	**O_2**	**NH_3**	**H_2O**	**OH**	**NO**	**H_2**	**H**	**O**
σ (10^{-27} cm^2)	5.61	4.88	8.98	3.90	8.34	5.51	1.17	0.83	0.96

4 Results and discussion

Results from the simultaneous PLIF measurements on the different burners are presented in this chapter. All of the selected cases are located in the regime of DRZ in the Borghi-Peters diagram. Image processing methods and procedures are also mentioned in this chapter. Meaningful information extracted from the images is used to complete further analysis of the flame structure and burning velocity.

4.1 Image processing schemes

Before presenting the results, details on the image processing methods are given. These schemes include NH layer thickness extraction, burning velocity evaluation, and conversion of Rayleigh signals to temperature.

4.1.1 **Procedures for PLIF results**

All the raw PLIF images have been processed using the following steps: 1) the average background noise, including the dark current in the ICCD cameras and the incident laser radiation, etc., was subtracted; 2) the nonuniformity of the laser power distribution was corrected by a vertical profile generated from the integration of the average signals along the horizontal direction; 3) A 3×3 median filtering process [68] was applied to smooth the images. After these standard processing procedures, images from one camera were registered to images from the other camera through a calibration target, matching the simultaneous measurements pixel-by-pixel, to produce overlapping images.

To extract the statistical quantities from the NH-PLIF images, further processing methods are required. The process to identify ridge lines and measure the NH layer thickness is depicted in Fig. 4.1. Except for the standard steps, the images were processed with morphological operations, binarised by a threshold [69, 70], and converted by a watershed transformation [71] to find watershed ridge lines marked by the red lines in Fig. 4.1c. Fig. 4.1d shows a partially enlarged view, the pixel distance between each point on the watershed ridge lines and the nearest point on the boundary in binary images [28] can be obtained easily and the NH layer thickness is defined as the 2 multiplying the pixel distance.

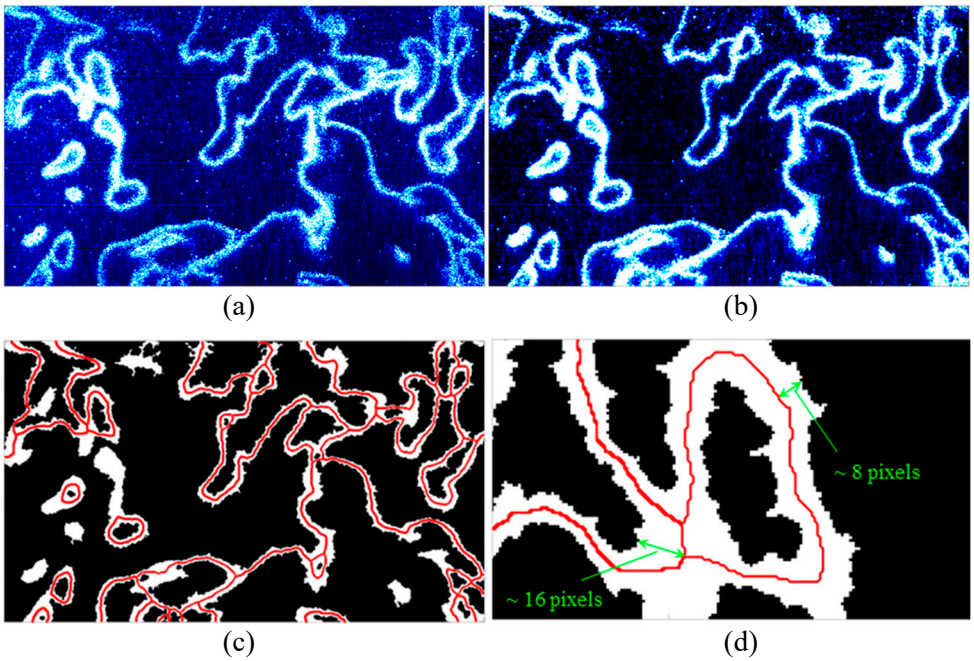

Fig. 4.1. A sample process of identification of ridge lines and NH layer thickness. (a) a raw NH-PLIF image, (b) result after standard processing, (c) ridge lines overlaid on the binarised image, (d) drawing of partial enlargement of (c).

The OH-PLIF visualisation has been widely used to estimate the turbulent burning velocity (S_T) since its leading edge is mostly located in the oxidation layer [9, 27, 35, 37, 38, 40]. When a series of instantaneous flame fronts are captured, the ensemble-averaged mean progress variable $\langle C \rangle$, indicating the probability that the certain point belongs to the burnt side, can be generated, as presented in Fig. 4.2. Binarisation of the OH-PLIF of the entire flame can be obtained following the same scheme as shown in Fig. 4.1. The leading edge is the boundary of the white and dark region, which is used to separate the burnt and unburnt areas. Fig. 4.2b shows the distribution of $\langle C \rangle$ from 250 instantaneous images and several iso-contour lines are plotted together. In order to obtain the turbulent burning velocity by equation (2.10), the mean flame surface area $\langle A \rangle$ has to be determined. The most convenient way in 2D measurements is to create a 3D model by rotating the iso-contour lines through the burner centre and use the surface area of the model to approximate $\langle A \rangle$ by assuming the flame to be axisymmetric. In this thesis, $\langle C \rangle = 0.5$ and $\langle C \rangle = 0.2$ will be employed, as in the work of Wabel et al. [35], which is aimed for a precise comparison of turbulent burning velocity in section 4.3.4.

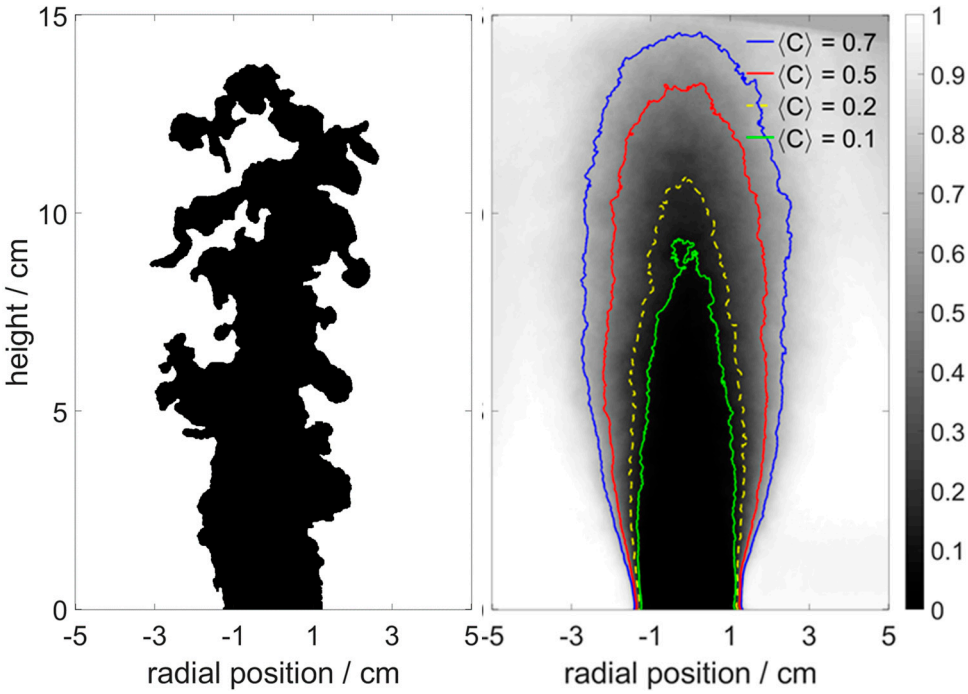

Fig. 4.2. (a) An example of OH binarised image, (b) Iso-contour lines of mean progress variable ⟨C⟩.

4.1.2 **Details for Rayleigh scattering images**

The Rayleigh signals were converted to instant temperature fields according to equation (3.6). The calibrated signals from pure nitrogen gas at 300 K were acquired to account for the reference parameters before measurement in ammonia flames. The remaining task is to determine the effective Rayleigh scattering cross section, which is an average value based on the composition of the mixture. However, the species and their mole fractions change greatly in a flame, as shown in Figs. 2.1 and 2.2. To address this problem, a structure of premixed laminar ammonia/air flame from the CHEMKIN simulations [14] at the same condition is needed to establish a connection between the species and the temperature distribution. The species considered in the calculation of the effective Rayleigh scattering cross section are listed in Table 3.2, and the result as a function of flame temperature is given in Fig. 4.3.

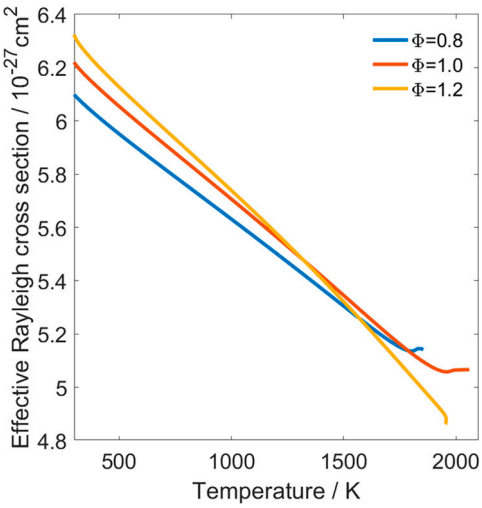

Fig. 4.3. Effective Rayleigh scattering cross section as a function of temperature in premixed laminar ammonia/air flames under different equivalent ratios.

As the function was generated, the final flame temperature can be obtained through several iterative steps, following the suggestion of Skiba et al. [67]: 1) the average background was removed; 2) the initial temperature field T_1 was solved by giving a random value of σ_{mix} and here the effective Rayleigh scattering cross section of the products was used; 3) the resulting temperature field T_2 was corrected (the point whose temperature larger than 3000K was set to 3000K) and this new distribution was utilised to update the σ_{mix}; 4) the resulting temperature field T_3 was compared with T_2 and the difference between two results was counted; 5) Steps 3 and 4 are repeated until the residual was stable; 6) the final temperature was filtered by a 3×3 median filtering.

4.1.3 **Verification of the processing methods**

To verify the accuracy of the processing methods, measurements from a laminar flame were taken first, and the measured reactive scalars were compared to those obtained from the CHEMKIN simulations.

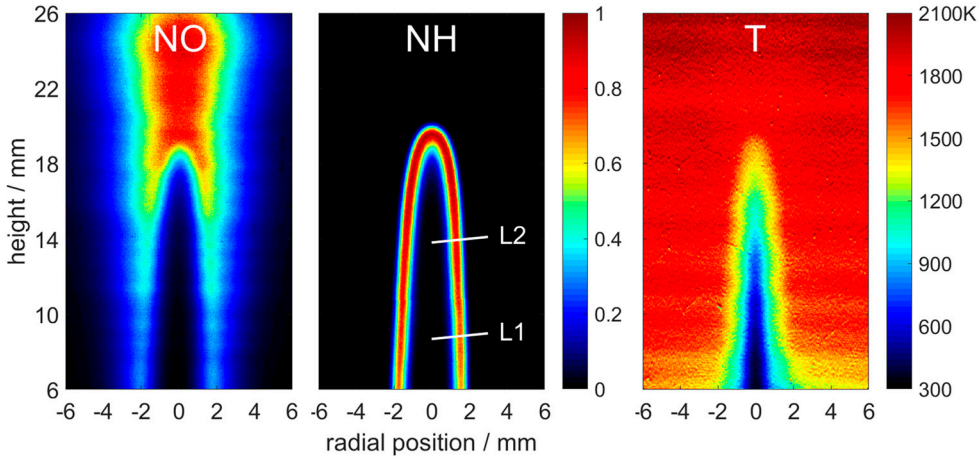

Fig. 4.4. Sample scalar images from a laminar NH_3/air flame with $\Phi = 1.0$.

Images of the laminar premixed ammonia/air flame at the stoichiometric ratio are shown in Fig. 4.4, which are an average of two hundred frames. The NH radicals located upstream from the NO region, with a thin layer, can be regarded as an indicator of the inner reaction layer [16]. In ammonia flames, NO is mainly formed in the reaction zone, and diffused axially and radially. Thus, the NO region has a wider span from the preheat zone, overlapping with the NH layer, and achieved equilibrium in the post-flame zone. A clear temperature gradient is observed close to the preheat and reaction region. Spatial profiles of the NH, NO PLIF signal, and the temperature recorded across two locations (L1 and L2 in Fig. 4.4) as well as along the centreline of the exit, are presented in Fig. 4.5a-c. Results of the CHEMKIN simulation, obtained from the one-dimensional freely propagating flame model [14], are plotted in Fig. 4.5d to make a comparison with the experimental data. The PLIF signals are normalised by their maximum values and the temperature profile was polynomial fitted. Profiles along the centreline have a qualitatively similar distribution to the simulated results. The inner layer marked by NH is located in the region where temperature is around 1500K in the experimental measurement. The peak of NO appears at the end of the NH layer and the signal intensity decreases radially with the effect of the pilot methane/air flame. The reason that the temperature profile is lower in Fig. 4.5a is likely due to the effect of reflections and scattering from burner surfaces, leading to increase of the Rayleigh scattering signal and the decrease of the evaluated temperature. Overall, the comparison reveals that measurements can provide reasonable results, giving solid support for the following turbulent analysis.

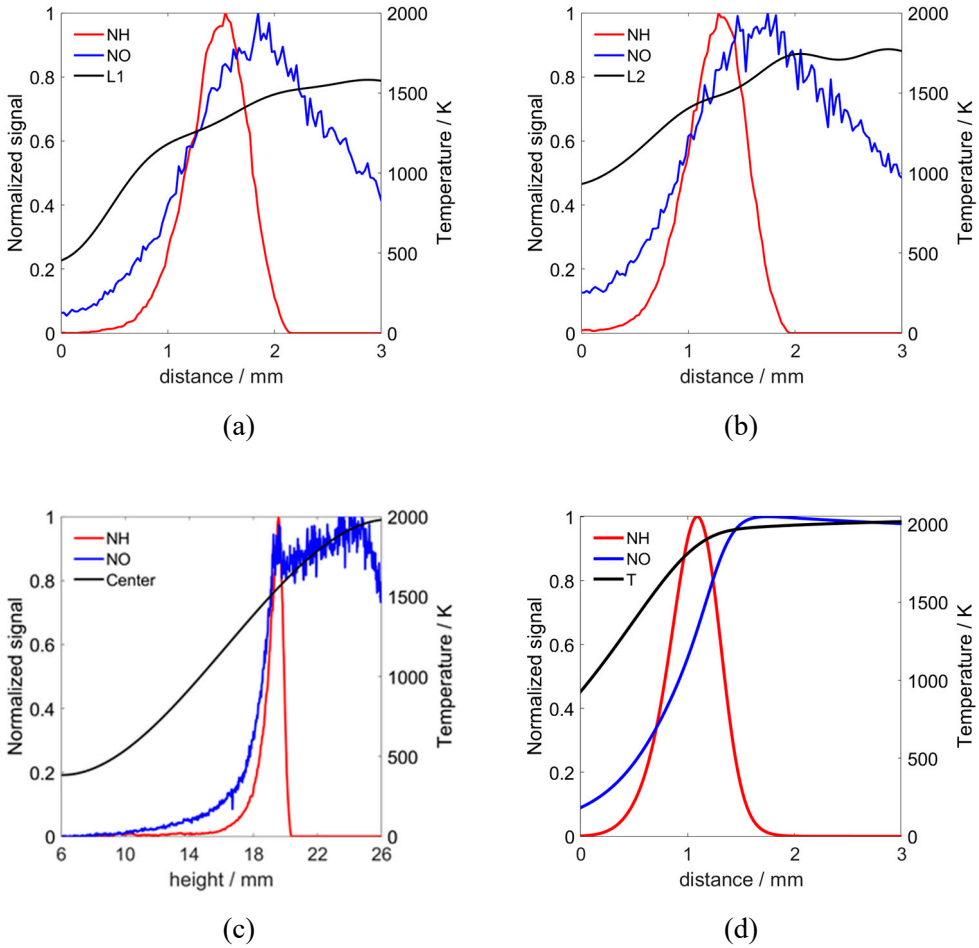

Fig. 4.5. Profile comparison of the reactive scalars between the experiment and CHEMKIN simulation. (a–b) along white lines L1 & L2 in Fig. 4.3, (c) along burner centreline, and (d) CHEMKIN simulation in number density.

4.2 Lab-scale jet flames (LUPJ burner)

Experiments on the fundamental characteristics of ammonia combustion have been carried out on the LUPJ burner (presented in Papers II and III). A series of lab-scale flames with a jet speed varying from 33 m/s to 220 m/s at the stoichiometric equivalent ratio are investigated using simultaneous PLIF and Rayleigh thermometry measurements. The instant distributions of the temperature (T) in

combination with the reactive NH radical or the NO pollutant are acquired. The flames are all located in the distributed reaction zones regime of the Borghi-Peters diagram shown in Fig. 2.4. Qualitative and quantitative analysis of the evolvement of flame structure is involved, and the experimental data are valuable for the model development.

Details of the investigated cases and their corresponding non-dimensional parameters related to turbulence and combustion are listed in Table 4.1. The values of turbulent velocity u' and integral scale l_0 are referred to the results of our previous LDA measurement [43]. The laminar flame speed and the laminar flame thickness are measured in laminar conditions.

Table 4.1 Details of the investigated turbulent flames

Cases	Jet speed (m/s)	Φ	S_L (cm/s)	δ_L (mm)	$\delta_{L,NH}$ (mm)	u' (m/s)	l_0 (mm)	Re_t	η (um)	u'/S_L	l_0/δ_L	Ka	Da
F1	33					3.3		82	106	49.8		274	0.033
F2	55					5.5		137	72	83.1		590	0.020
F3	110	1.0	6.62	1.76	0.64	11	2.9	299	40	181.3	1.65	1900	0.010
F4	165					16.5		411	32	249.2		3065	0.007
F5	220					22		548	26	332		4720	0.005

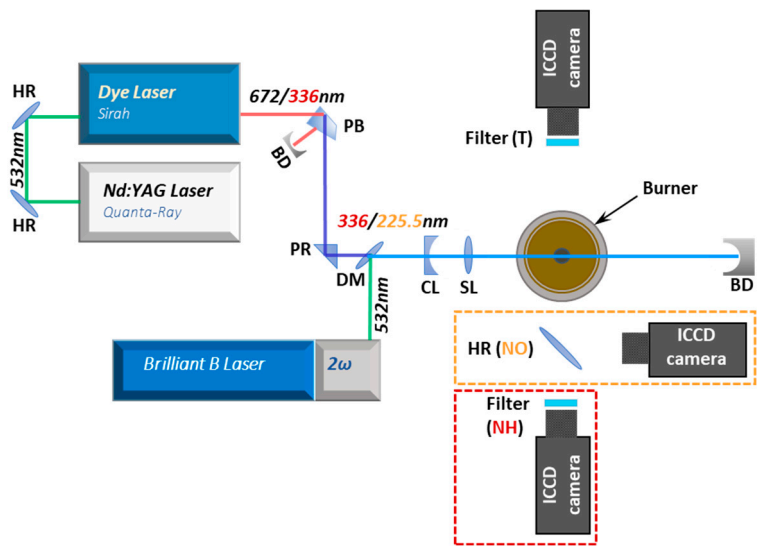

Fig. 4.6. Experimental setup for simultaneous scalar measurements of the LUPJ flames.

The schematic of the experimental setup is shown in Fig. 4.6. Two laser systems were employed for the synchronised NH/NO and T imaging. A dye laser was tuned to 336 nm and 225.5 nm for NH and NO excitation, respectively. A

Nd:YAG laser was operated at 532 nm for the Rayleigh scattering thermometry. The laser beams were overlapped and shaped into a 3 cm high, 200 μm thick laser sheet by a sheet-forming system. The resonant signal of NH radicals was collected by an ICCD camera, equipped with a UV lens and a UG11 filter. The NO fluorescence was acquired through a narrow band dichroic reflection mirror to avoid the scattering interference. The Rayleigh scattering signals were measured by another ICCD camera mounted with an objective (f = 105 mm, f/2.5, Nikon) and a bandpass filter (532 ± 10 nm).

4.2.1 **Multi-scalar imaging**

Fig. 4.7 shows groups of simultaneous single-shot images of NH/T distribution with various jet speeds. The NH layer of cases F1 and F2 shows wrinkled and corrugated as located in the flamelet mode, although the Ka number is already larger than 100 and the Kolmogorov scale η is much smaller than the NH layer thickness. A strong correlation between the NH radicals and a relatively high-temperature region (> 1500K) can be found easily. The flame structure becomes more complicated and the NH layer is thickened locally when the jet speed is higher than 110 m/s. Clear broadening is observed at the flame tip, which is a comprehensive result of the turbulence/flame interaction, merging of the flame front, and 3D effects.

The preheat zone corresponds to the region separated by the NH radicals close to the reactant side, and is broadened greatly due to intense mixing of reactants/products and the transfer of heat when the Ka number increases. Compared with case F1, the preheat zone of flame F5 is quite wide and extended along the radial direction at the same height. Previous studies of high Ka flames have shown that the thickness of the preheat zone is proportional to the integral length of turbulence eddies rather than the jet speed [37]. It seems that the effect of turbulent eddies is more dramatic in the preheat zone than the reaction zone (i.e., the NH layer), which is consistent with the findings in methane/air flames [24, 48]. Another experimental result shows that the Kolmogorov eddies have been significantly dissipated when penetrating the preheat layer [52].

For flame F5, with jet speed reaching 220 m/s and a Ka number as high as 4720, the NH layer shows local discontinuities as local flame extinction happens (cf. flame height around 62 mm). This is attributed to the low temperature gas involved in flames. At such high speed, the pilot flame is not strong enough to prevent cold air entrainment to the jet flame, causing the phenomenon of flame quenching.

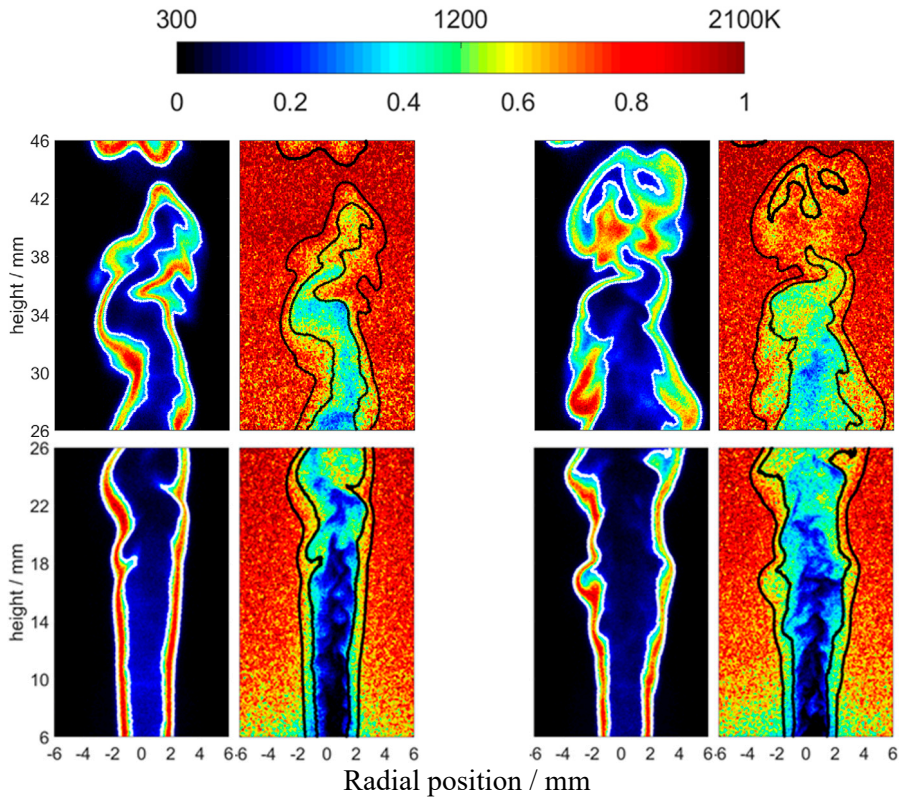

(a) F1 33m/s (b) F2 55m/s

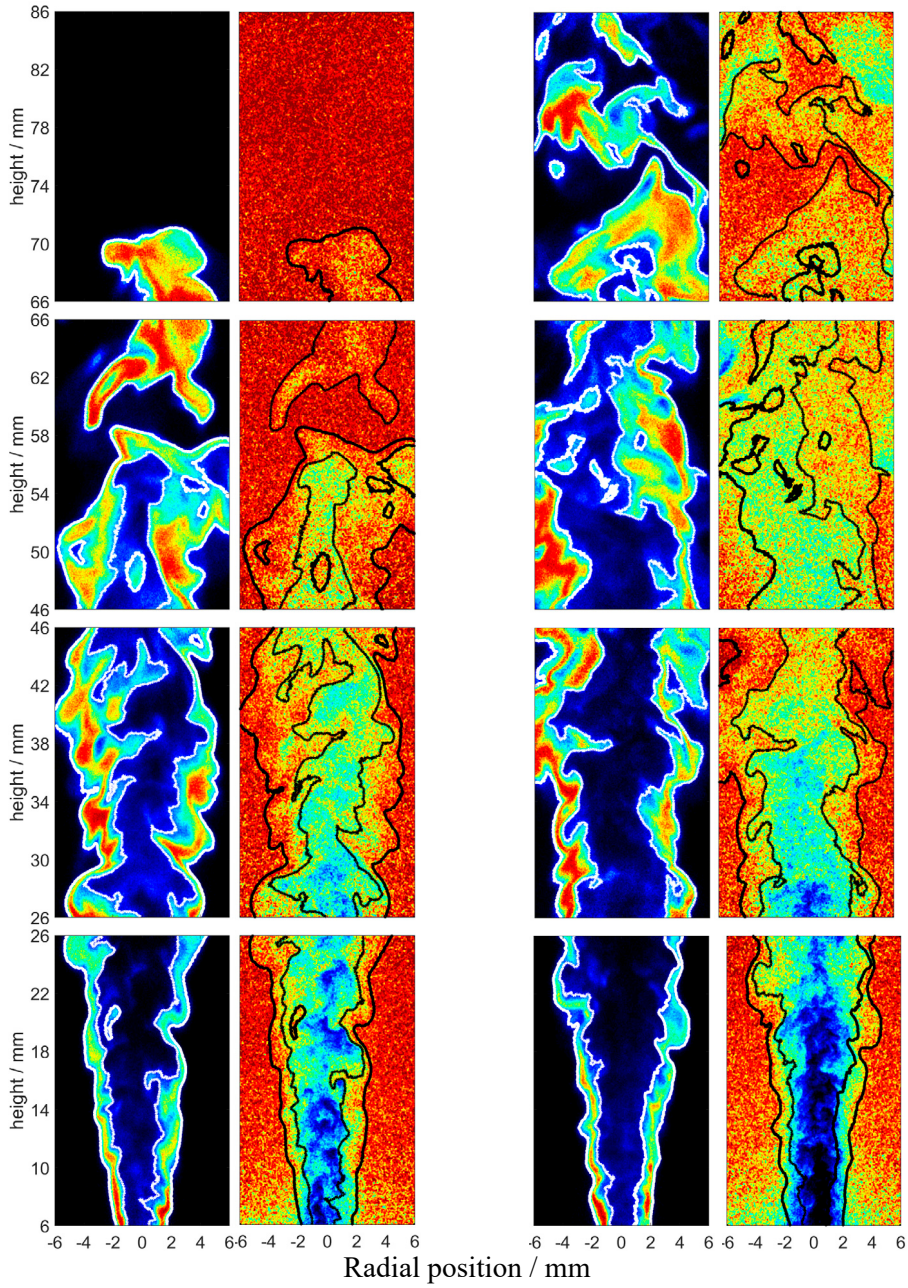

(c) F3 110m/s (d) F5 220m/s

Fig. 4.7. Simultaneous single-shot images of NH/T distribution for the selected cases. Edges from the NH binary images were superimposed on the results.

Fig. 4.8 shows representative single-shot images of simultaneous NO/T distribution with the selected cases. A wider NO region is noticed in high Ka number, turbulent premixed ammonia/air flames. The broadening of the NO distribution can be attributed to three factors: 1) the broadened NO formation layer, due to the broadening of the NH layer; 2) the turbulence-enhanced diffusion of NO to the preheat zone; and 3) the enhanced transport of NO to the post-flame zone. Low signal regions of NO at post-flame zone are observed, e.g., flame F1 (flame height 42 – 44 mm) and flame F3 (flame height 58 – 66 mm). This arises from the large-eddy transport of hot gas from the pilot flame, which produces less NO in methane/air flames. In flame F4, at a height of around 82 mm, one can observe a cold spot with a low NO concentration. This region corresponds to the cold air entrained by the high-speed jet flow.

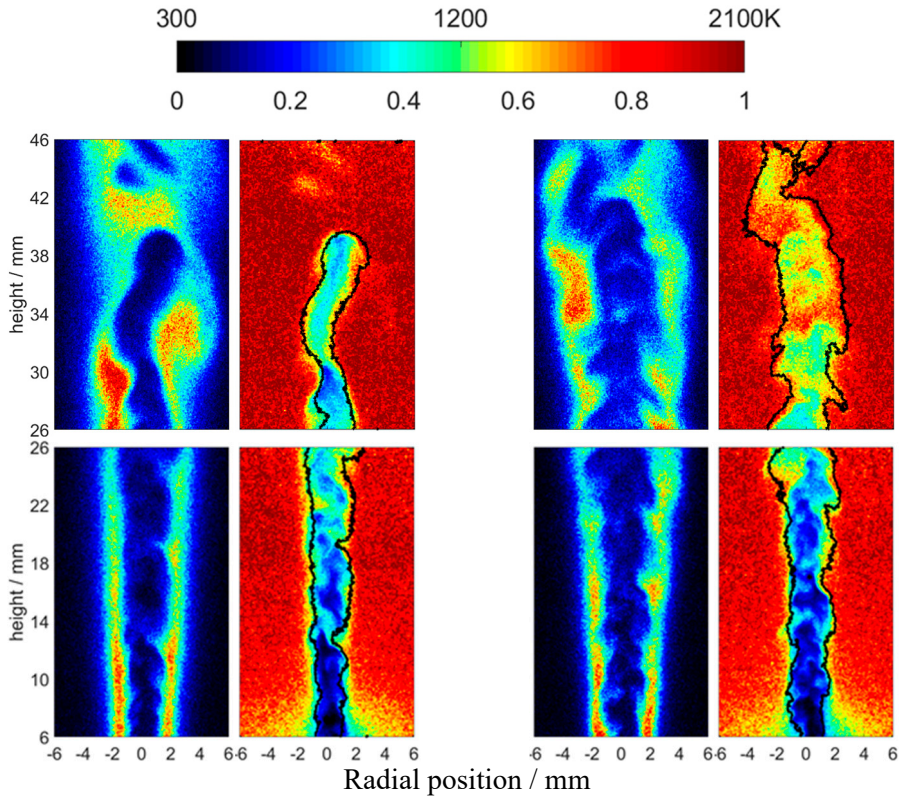

(a) F1 33m/s (b) F2 55m/s

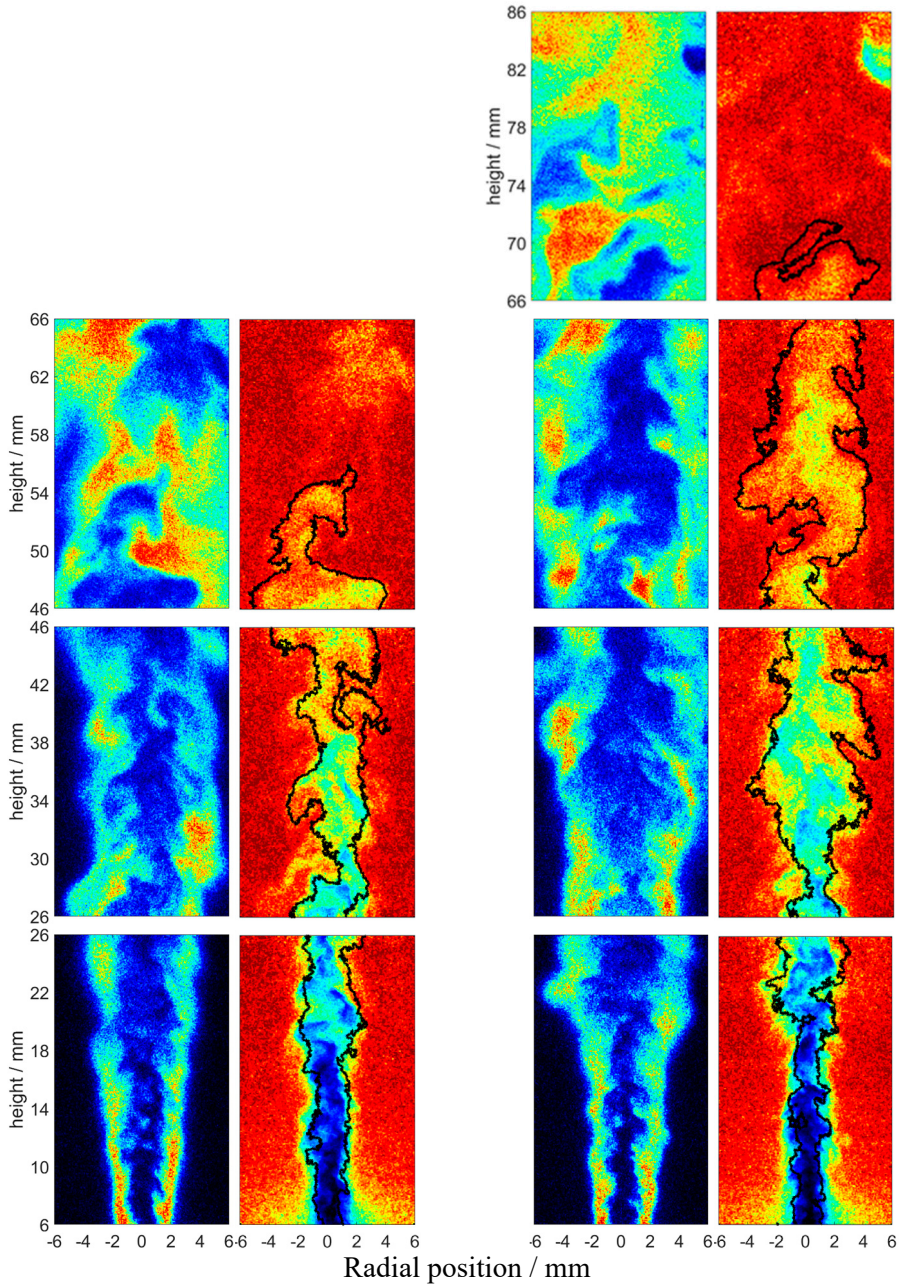

(c) F3 110m/s (d) F4 165m/s

Fig. 4.8. Simultaneous single-shot images of NO/T distribution for the selected cases. The leading edge from the NO binary images was superimposed on the temperature results for comparison.

4.2.2 **Statistical analysis of the flame structure**

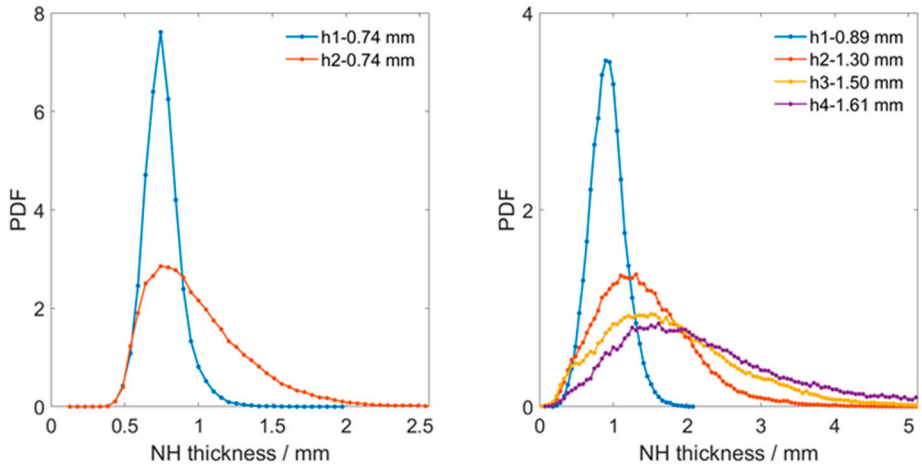

(a) F1 (b) F5

Fig. 4.9. PDF of NH layer thickness at different regions in cases F1 and F5. Flame regions: h1=10–20 mm, h2=30–40 mm, h3=50–60 mm, and h4=70–80 mm. The legend indicates the NH layer thickness at the peak value.

The above discussion of NH-PLIF is only based on single-shot images, and the turbulent flame structure changes significantly from shot-to-shot. Statistical analysis of the variation of NH layer thickness is required for further study. Fig. 4.9 shows the probability density function (PDF) of the NH layer thickness at different regions of cases F1 and F5. The most probable value of the PDF is used to represent the NH layer thickness indicated in the legend. In general, the thickness of the NH layer increases with the turbulent intensity (u'/S_L) and the flame height. The profiles of the PDF have a similar distribution in the first flame region (h1 = 10–20 mm), which can be seen from the NH-PLIF images shown in Fig. 4.7. Actually, the NH layer remains thin in all results at the low flame height because of the small integral length scale around burner exit [37]. In the development of turbulence in F5, a significant broadening about three to four times of the NH layer can be observed downstream, although the peak values of PDF are skewed towards the thin side. The criterion of $Ka \approx 100$ used in methane/air flames is not applicable in the present ammonia/air flames, indicating that regime classification should take the fuel type into consideration.

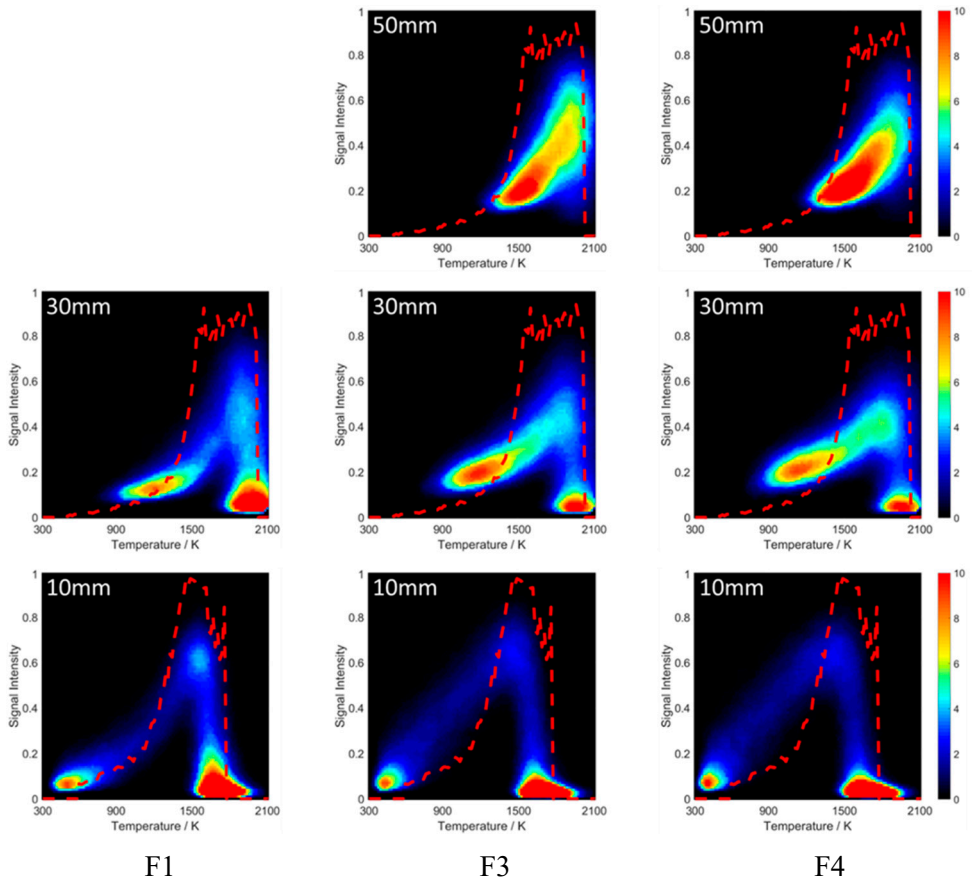

Fig. 4.10. NO/T JPDF for selected flames, F1, F3, and F4 at different flame heights. The colorbar represents the values of the JPDF; the red dashed lines are the correlations in laminar flame.

The joint probability density function (JPDF) of NO and T for the selected flames at different heights is presented in Fig. 4.10, which is used to quantify the interaction of turbulence/chemistry. Three regions with high values of JPDF can be recognised at the first height: the low temperature region with low NO intensity corresponds to the preheat zone; the high temperature region with low NO intensity corresponds to the hot gas mixture from the pilot flame; and the NO peak is at intermediate temperature, which is the NO formation region in the reaction layer. As the flame height increases to 30 mm, the high values of JPDF in the preheat zone are shifted to higher temperatures due to the heat and mass enhancement from the reaction zone. When the height is 50 mm, in cases F3 and F4, the peak JPDF regions in the preheat and reaction zones are merged, and the

high-temperature and low-NO region disappears. Compared with the laminar flame profile, the NO intensity is lower in high Ka flames, which may be attributed to the broadened reaction zones in the turbulent flames.

4.3 Large-scale Bunsen flames (DRZ burner)

To extend the investigation of turbulent ammonia combustion closer to industrial application level, for example, at stationary gas turbines under premixed conditions [4, 72], experiments have been performed on the DRZ burner (presented in Paper I). The structure of the premixed ammonia/air flame was visualised by simultaneous two-species PLIF (NH/OH) and Laser Doppler Anemometry (LDA), to measure the relevant turbulent quantities from the flow field. A schematic of the experimental setup is shown in Fig. 4.11 and the layout of the whole system in the lab is presented in Fig. 4.12. A dye laser system was tuned to 607.15 nm and the generated beam at 303.576 nm was used to excite the NH radicals. Details of the excitation-detection strategy can be found in Ref. [73]. The OH excitation was performed at 283.5 nm by another dye laser system. Two laser beams were guided to overlap, and were expanded to sheets using a sheet-forming optics system. The fluorescence of the NH signal was collected by a PI-max 3 ICCD camera mounted with a UV objective and a long-pass filter (WG335, Schott). The OH fluorescence signal was detected by a PI-max 2 ICCD camera equipped with a UV lens and a 320 ± 20 nm bandpass filter. To keep synchronised, all the systems were triggered by a digital pulse generator. To visualise the complete flame profile in one single image, a divergent laser sheet as large as 15 cm, covering the whole flame region, was created for individual OH-PLIF measurements. The results will be used to estimate the turbulent burning velocity (S_T).

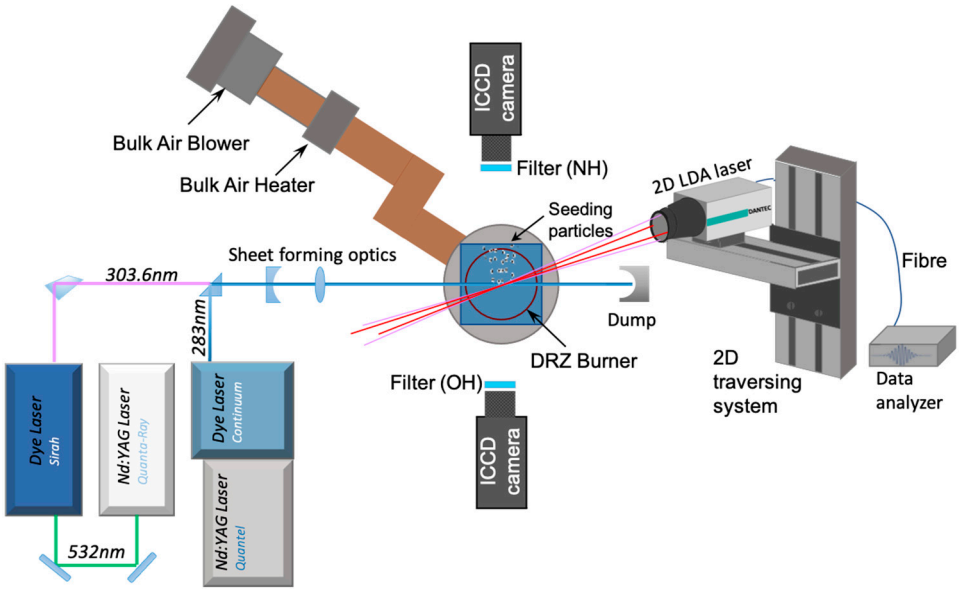

Fig. 4.11. A schematic of the experimental setup.

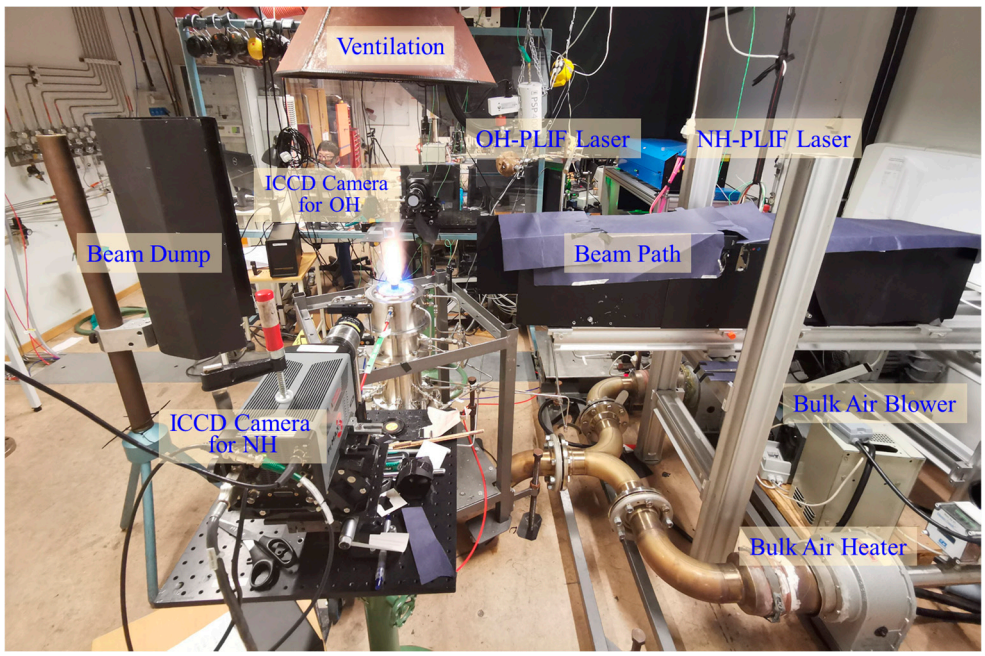

Fig. 4.12. A photograph of the whole system in the atmospheric rig.

Table 4.2 shows the details of the turbulent flame conditions in the investigation. Cases are referred to as DRZα-β, where α indicates the value of equivalence ratio Φ of the flame and β represents the jet flow velocity. Nine cases with a bulk flow speed ranging from 10–30 m/s and three different equivalence ratios (Φ = 0.8, 1.0, 1.2) are included. The pilot CH_4/air flame (Φ = 1.0) has an inlet velocity of approximately 0.9 m/s. The laminar flame speed (S_L), laminar flame thickness (δ_L), and NH layer thickness ($\delta_{L,NH}$) were obtained from numerical simulations based on a CH_4/NH_3 mechanism of Okafor et al. [74]. $\delta_{L,NH}$ is the full width at half the maximum (FWHM) of the NH profile. The turbulent velocity (u') and integral length scale (l_0) were obtained from LDA measurements, and the values in Table 4.2 were the results obtained at 10 mm above the centre of the burner exit. Detailed description are provided in section 4.3.1. The range of the turbulent intensities (u'/S_L) can be observed to range from 58 to 240, corresponding to a Reynolds number of 836 to 3274, and the integral length scales are 30 – 40 mm.

Table 4.2 Conditions of the investigated turbulent flames.

Cases	Φ	S_L (cm/s)	δ_L (mm)	$\delta_{L,NH}$ (mm)	u' (m/s)	l_0 (mm)	Re_t	η (um)	u'/S_L	Λ_0/δ_L	Ka	Da	LDA
DRZ08-10	0.8	4.06	2.89	0.66			1026	162	101	10	320	0.100	
DRZ10-10	1.0	6.92	1.95	0.67	4.11	29.30	892	179	59	15	118	0.253	√
DRZ12-10	1.2	7.03	2.05	1.29			836	189	58	14	118	0.244	
DRZ08-20	0.8	4.06	2.89	0.66			2139	112	176	12	667	0.069	
DRZ10-20	1.0	6.92	1.95	0.67	7.13	35.20	1860	124	103	18	246	0.175	√
DRZ12-20	1.2	7.03	2.05	1.29			1741	131	101	17	246	0.169	
DRZ08-30	0.8	4.06	2.89	0.66			3274	91	240	14	1008	0.057	√
DRZ10-30	1.0	6.92	1.95	0.67	9.75	39.40	2847	101	141	20	372	0.143	√
DRZ12-30	1.2	7.03	2.05	1.29			2666	106	139	19	373	0.139	√

4.3.1 **Flow field characterisation**

In the LDA measurements, burst mode sampling is used for the data collection, which can provide high temporal resolution. Two channels for two velocity components run in a coincidence mode. The recorded length of each burst is auto-adaptive according to the number of recorded samples and local velocity. The detected result is validated by the specified ratio between the 1st and 2nd peak from the frequency spectrum using the Fast Fourier Transform (FFT) algorithm.

To extract relevant turbulence information, the LDA measurements were conducted in five cases, reported in Table 4.2. The velocities of the whole flow field were measured by scanning the probe volume from 10 mm to 150 mm above the jet exit, with a step 20 mm along the axial direction, and an adaptive step along the radial direction, totalling 20000 data points collected in each position. To avoid statistical bias, average quantities, such as mean velocity U and root-mean-square (rms) velocity fluctuation σ, are calculated by transit time weighting:

$$U = \sum_{i=0}^{N-1} \eta_i U_i \tag{4.1}$$

$$\sigma = \sqrt{\sum_{i=0}^{N-1} \eta_i (U_i - U)^2} \tag{4.2}$$

The weighting factor η_i is the ratio between transit time at each point and sum of the total transit time, and U_i is the transient velocity at each dimension. The distribution of mean axial velocity, U(x, r), along the radial direction at different heights above the burner in two different cases, is shown in Fig. 4.13a-b. Fig. 4.13c-d shows the profile of mean axial velocity and turbulent velocity along the centre line of the burner, which is normalised by the value U_0 taken at 10 mm above the centre jet, and the normalised turbulence velocity I is calculated by:

$$\mathrm{I} = u'/U_0 \tag{4.3}$$

$$u' = \sqrt{\frac{1}{3}\left(\sigma_x^2 + 2\sigma_y^2\right)} \tag{4.4}$$

where σ_x and σ_y are the axial and radial rms velocity fluctuations, respectively, with the assumption that the fluctuated velocity in the tangential direction is equal to the radial fluctuated velocity.

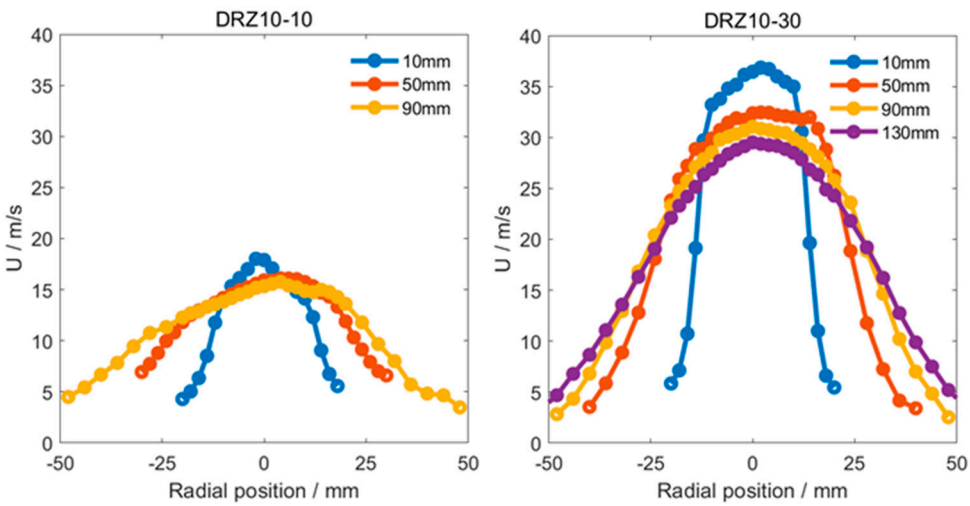

(a) (b)

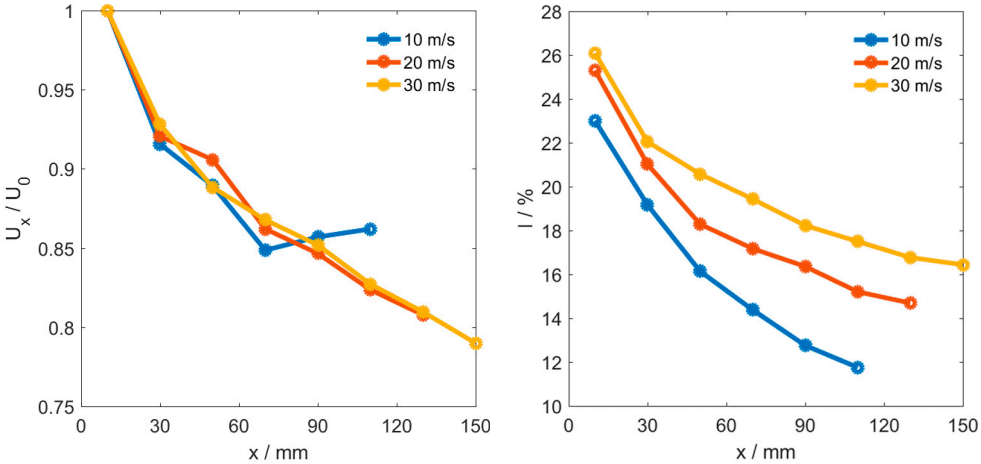

Fig. 4.13. (a-b) Mean axial velocity distribution along the radial position at different heights above the burner exit plane. (c-d) Distribution of the normalised axial velocity and the normalised turbulence velocity along the flame height.

The axial velocity decreases monotonously with the increasing burner height for the 20 m/s and 30 m/s cases, while the 10 m/s case shows a nearly constant axial velocity distribution between 60 mm to 100 mm from Fig. 4.13c. This is attributed to the low turbulent velocity u' and the thermal expansion, because the flame height in this case is shorter compared to the other two cases. The normalised mean axial velocity of the 20 m/s and 30 m/s cases overlap very well, indicating that the flow fields of the two cases are close to being self-similar. The normalised turbulence velocity in the proximity of the burner is rather similar (approximately 24 – 26%), indicating a well-developed turbulence field inside the burner.

Unlike the average quantities, the investigation of time-correlation and spectrum requires high data rate, and this is achieved by increasing the amount of seeding and the sensitivity of the signal amplifier with a sacrifice of the validation. 10^5 samples are recorded in the centre of the burner at each 10 mm height, with a validation higher than 80% and the maximum data rate up to approximately 20 kHz. The time auto-correlation function and power spectral density are calculated by the FFT techniques. The raw samples are resampled and spaced equally in time before doing FFT-analysis, and these processed data are divided into consecutive blocks in the equal lag-time, so the final correlation is an average value in the total acquisition time. As our collection rate was about 20 kHz in each case, the number of samples is set to 1024 with a maximum 50 ms lag-time. This lag-time is almost 100 times the integral time scale, which can provide reasonable results.

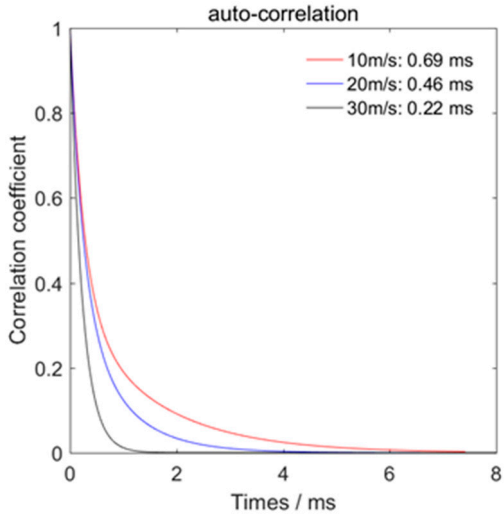

Fig. 4.14 The auto-correlation for the three cases

The autocorrelation in turbulent flow is used to describe how the eddy structures can last in the time or the space scale. Fig. 4.14 shows the fitted autocorrelation function of the three different jet velocities under the equivalence ratio of 1, and their axial integral time scales τ_0 are also given in the legend. Lines are fitted using an exponential function, keeping the coefficient equal to one at which the lag-time Δt is zero. With the lag-time increasing, the auto-correlation decays to zero rapidly. The integral time scale τ_0 is the integration of this fitted curve over the lag-time, which represents the turnover time of the large eddies. As the jet speed gets faster, the turbulent velocity increases, leading to the decrease of the integral time scale. These time scales are often converted to the axial integral length scale l_0 by the corrected version of Taylor's frozen-flow hypothesis [75, 76]: $l_0 = \tau_0 U \left(1 + \frac{\overline{\sigma_x^2}}{U} + 4\frac{\overline{\sigma_y^2}}{U^2}\right)$ and the results are listed in Table 4.2 to characterise the interaction between turbulence and chemistry.

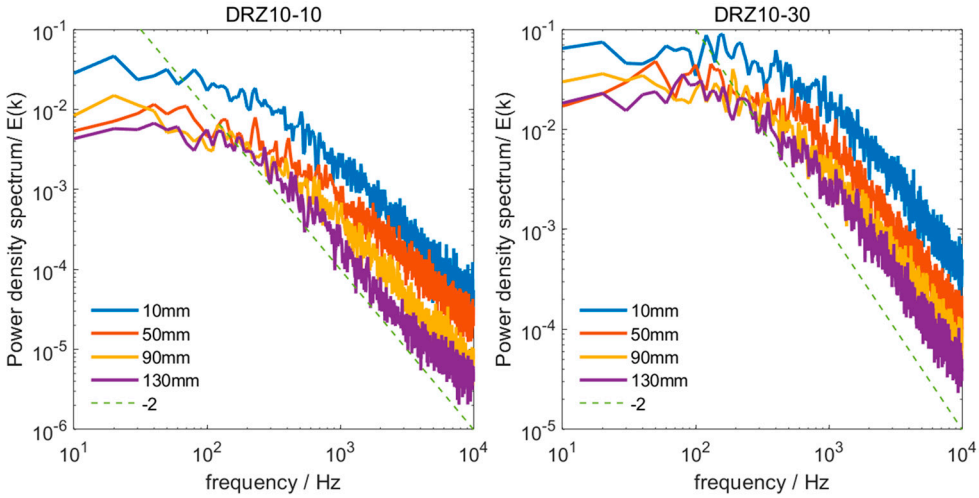

Fig. 4.15 Turbulent power density spectrum against the frequency at different heights for two different cases.

The power density spectrum (PDS) of the turbulent fluctuation based on jet speed 10 m/s and 30 m/s with four different heights is shown in Fig. 4.15. All the data are collected longer than 5 s, which means that the minimum PDS frequency can be 0.2 Hz and the maximum frequency is limited by our data rates and the Nyquist frequency [77]. The dashed line in each figure represents an arbitrary power function whose exponential value is -2. The result shows that the spectral power starts to decay with f^{-2} [23] as the frequency increases to a critical frequency, and this frequency is the start point of the inertial subrange. This can be explained as the kinetic energies $(u')^2$ of eddies in this region being inversely proportional to the frequency, as [24]:

$$(u')^2 \sim \varepsilon f^{-1} \tag{4.5}$$

Thus, the power density spectrum in the frequency space can be expressed as:

$$\mathrm{E}(\kappa) = \frac{d(u')^2}{df} = C\varepsilon f^{-2} \tag{4.6}$$

In most literatures, this relationship is expressed in wave-number form, known as $k^{-5/3}$ law.

This critical value is very similar to the large eddy turnover frequency (u'/L_x) which is 140 Hz for 10 m/s and 247 Hz for 30 m/s, respectively. For frequencies lower than this value, the PDS in the energy-containing range has a flat

distribution without any viscous dissipation or energy transfer. As the flow velocity increases, the time scale of the eddies is broadened and more turbulent kinetic energy is transferred from the main flow.

4.3.2 **Single-shot imaging**

Examples of the flame structure visualised by simultaneous NH/OH PLIF for different flames are shown in Figs. 4.16, 4.17 and 4.18. The left column is the NH PLIF and the corresponding OH regions are listed in the middle. The overlap results of the NH distribution and the OH leading edge with red lines are given in the right column.

The NH layer remains continuous and thin in all three cases. However, the flame structure is wrinkled and corrugated due to the interaction between eddies and flame as the jet speed increases. The fuel-consumption layer, indicated by the NH radicals, is not broadened although the Ka has reached 1008 in Fig. 4.18. The results demonstrate that flames still resemble those in the thin reaction zone regime while the Kolmogorov scale in case DRZ08-30 is 91 μm, which is about 1/5 of the thickness of the NH layer in Table 4.2. The criterion suggested, using Ka = 100 to separate the thin reaction zone and the distributed reaction zone regimes, needs further revision.

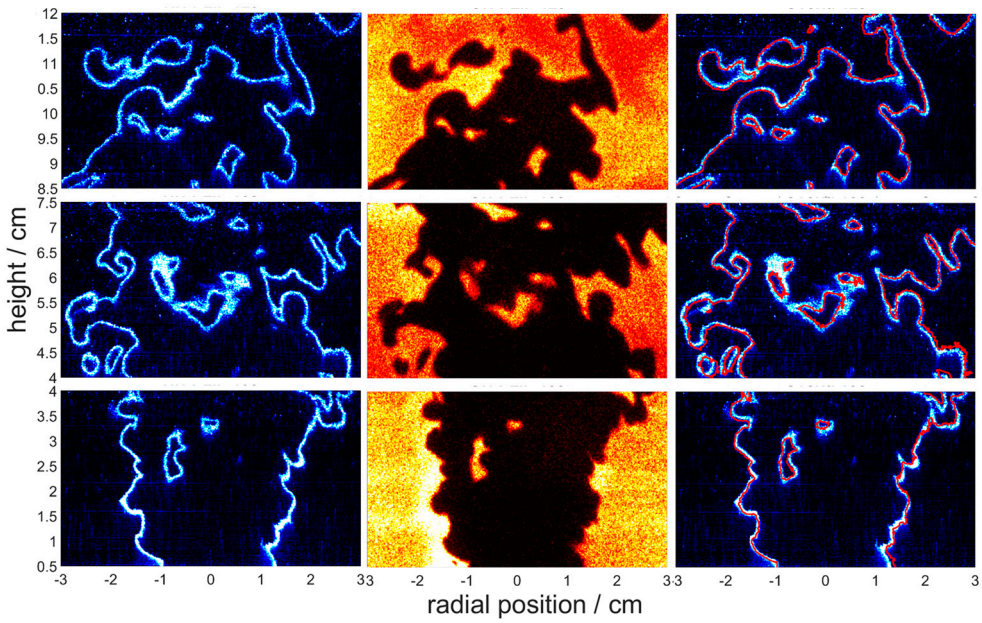

Fig. 4.16. Simultaneous single-shot images of NH PLIF (left), OH PLIF (middle), and the inner edge of OH overlaid on NH PLIF field for Case DRZ10-10.

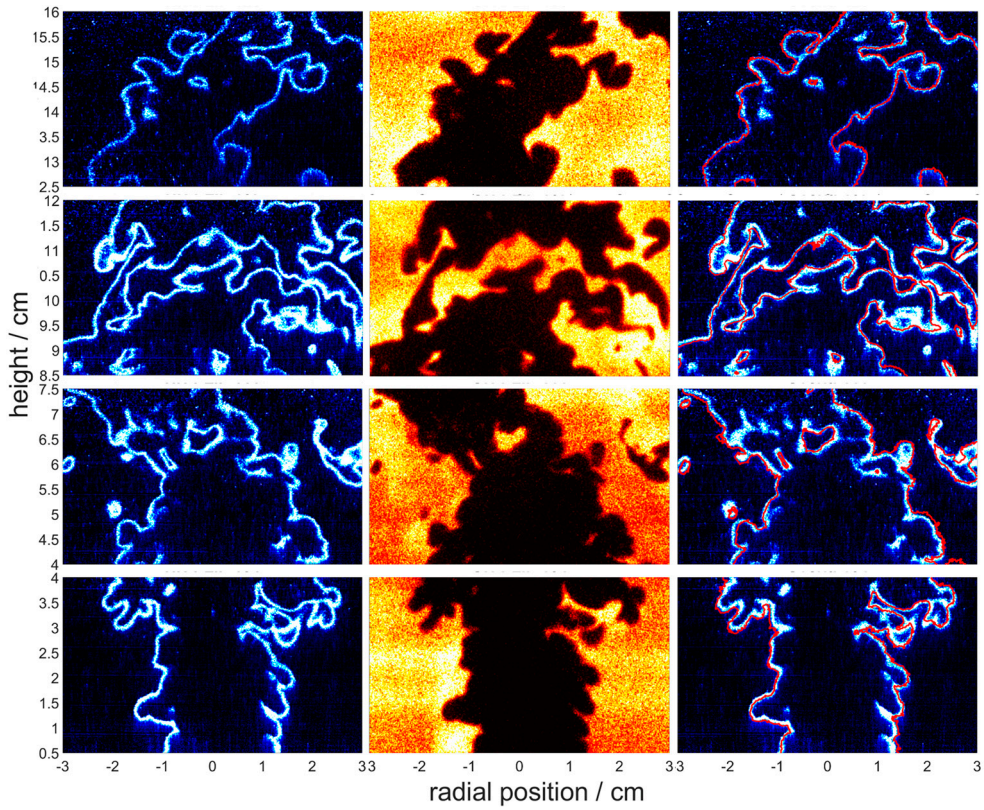

Fig. 4.17. Simultaneous single-shot images of NH PLIF (left), OH PLIF (middle), and the inner edge of OH overlaid on NH PLIF field for Case DRZ10-20.

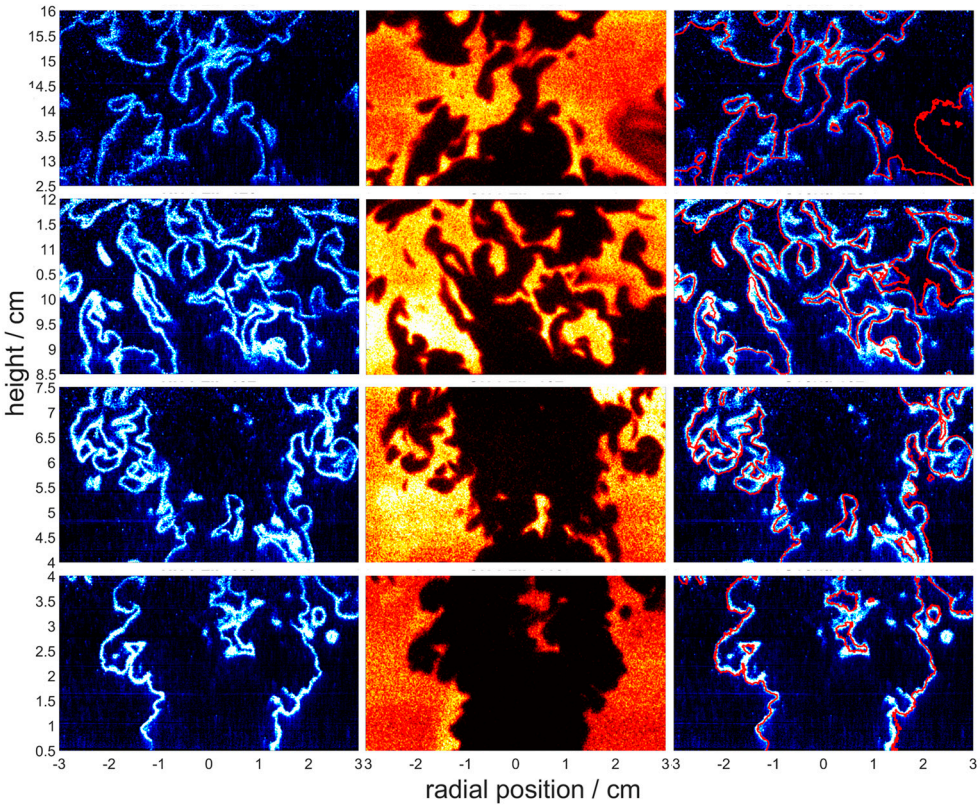

Fig. 4.18. Simultaneous single-shot images of NH PLIF (left), OH PLIF (middle), and the inner edge of OH overlaid on NH PLIF field for Case DRZ08-30.

The unburned reactants are enclosed by the OH radicals and the leading edge (marked as the red lines) is overlaid on the NH field. The inner edge of OH-PLIF and the NH layer coincide with each other in a thin area where the OH has a weaker signal intensity. This distribution is consistent with the corresponding species profiles in Fig. 2.2. Pockets of products exist in the unburned region and these island formations are likely due to the 3D wrinkled flame surface. Local extinction happens at the top of Fig. 4.18, where the signal intensities of both NH and OH decrease because of the entrainment of cold air.

4.3.3 **NH layer thickness**

Fig. 4.19 presents the ensemble-averaged mean thickness of the NH layer from 250 images for all selected cases in Table 4.2. The NH layer remains thin and does not vary much with the flame height, as well as with the wide range of turbulent

intensities, which is consistent with the findings in Figs. 4.16, 4.17, and 4.18. The fuel-rich flames with Φ equal to 1.2 show a much thicker NH layer than the lean and stoichiometric conditions. This difference can be attributed to the following factors: the influence of the equivalence ratio shown in Table 4.2 from the laminar flame CHEMKIN simulations, the NH PLIF signal detection that low-intensity signal may not properly capture, the binarisation of the signal, and the finite resolution limits. The result confirms that the NH layer is not statistically broadened by turbulence eddies under high Ka conditions.

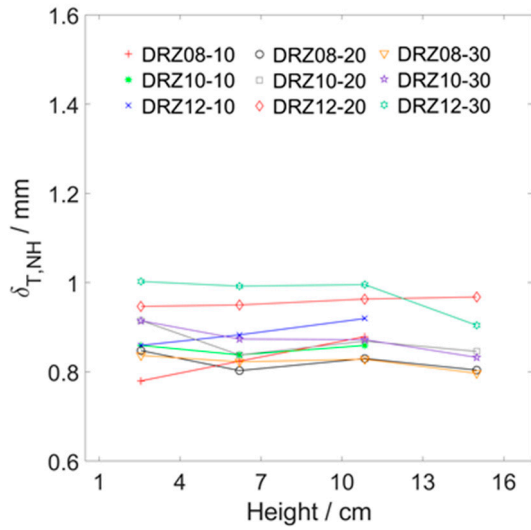

Fig. 4.19. The mean NH layer thickness at different heights for all cases.

4.3.4 **Turbulent burning velocity**

The turbulent burning velocity (S_T) calculated from equation (2.10) for nine cases is shown in Fig. 4.20. The result calculated by $\langle C \rangle = 0.2$ is about two times that of $\langle C \rangle = 0.5$, which is the same as findings in methane/air flames by Wabel et al. [35]. It is clear to observe that the S_T of the ammonia flames is lower than that of the methane flames under the same turbulent intensities, which is the same as the result of Ichikawa et al. [9]. The turbulent burning velocities present a linear increase with the turbulent intensity in our study. This trend is consistent with the local flamelet-like behaviour [39], which has been proven by the thin NH layer at high Karlovitz numbers in section 4.3.2 and 4.3.3. To understand the mechanisms of the flame propagation, further analysis on the effect of turbulent intensity on the flame surface is needed.

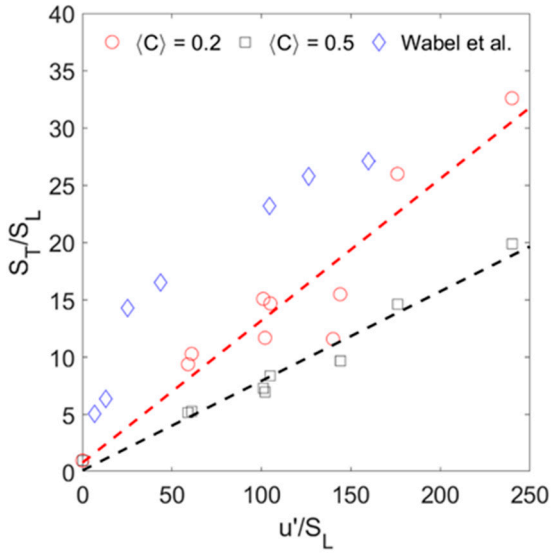

Fig. 4.20. Turbulent burning velocity normalised by the corresponding laminar value as a function of turbulent intensity (u'/S_L) for flames in Table 4.2. The data for methane/air flames from Wabel et al. [35] are also plotted for comparison.

In the flamelet regime, the turbulent burning velocity is proportional to the flame surface density (FSD, Σ) in Equation (2.11), which is defined as the flame surface area in a unit volume in space.

$$S_{T,LC} = S_L I_0 \int_{-\infty}^{+\infty} \Sigma dx_n \tag{4.7}$$

The integral part is the ratio of wrinkled flame surface area A_T to that of the mean flame brush $\langle A \rangle$.

$$\int_{-\infty}^{+\infty} \Sigma dx_n = \frac{A_T}{\langle A \rangle} \tag{4.8}$$

Thus,

$$\frac{S_T}{S_L} = I_0 \frac{A_T}{\langle A \rangle} \tag{4.9}$$

In the 2D measurements, the FSD is the ratio between the length of the flame segment and the area of the interrogation window.

$$\Sigma = \frac{L}{(\Delta x)^2} \tag{4.10}$$

where L is the length of the flame surface in an interrogation window and Δx is the side length of this window. Three different interrogation windows with a size of Δx varying between 0.5 and 1.5 mm were considered to eliminate the effects of variation of window size and an area of 15 × 15 pixels was finally chosen. This is shown in Fig. 4.21. The distribution of Σ along the radial position coincides very well with fewer changes, indicating that Σ is independent of the window size.

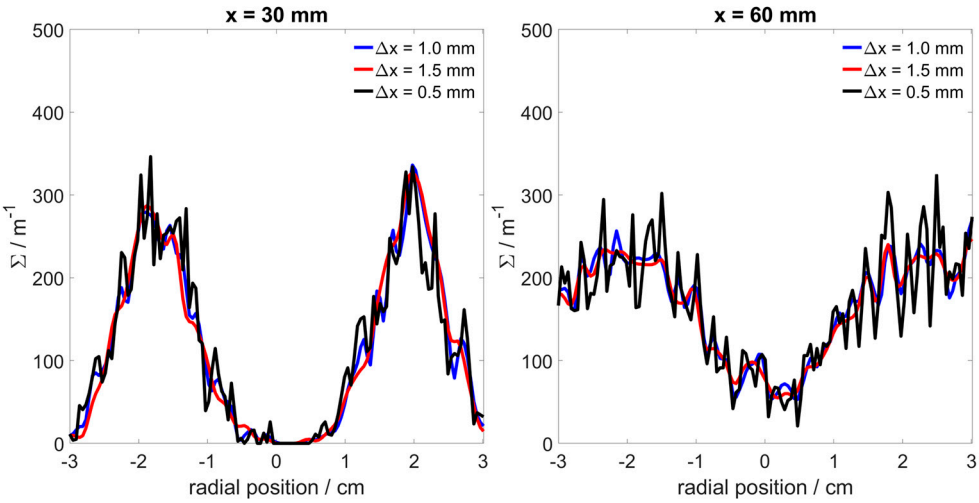

Fig. 4.21. Variation of Σ for case DRZ10-30 based on OH-PLIF at two flame heights.

The average of results from 250 OH-PLIF images of the relation between the flame surface density (FSD, Σ) and mean progress variable $\langle C \rangle$ is shown in Fig. 4.22. The data were fitted with a dashed line by a polynomial. The Σ has a similar distribution for all conditions and seems independent of the Karlovitz number. The peak of Σ decreases at approximately $\langle C \rangle$ = 0.5 as the flame height increases from 30 mm to 60 mm because the extensive space of the mean flame brush is broader than that at lower flame height, indicated by Figs. 4.2b and 4.21. This result is in agreement with the DNS of V-flames published by Domingo et al. [78].

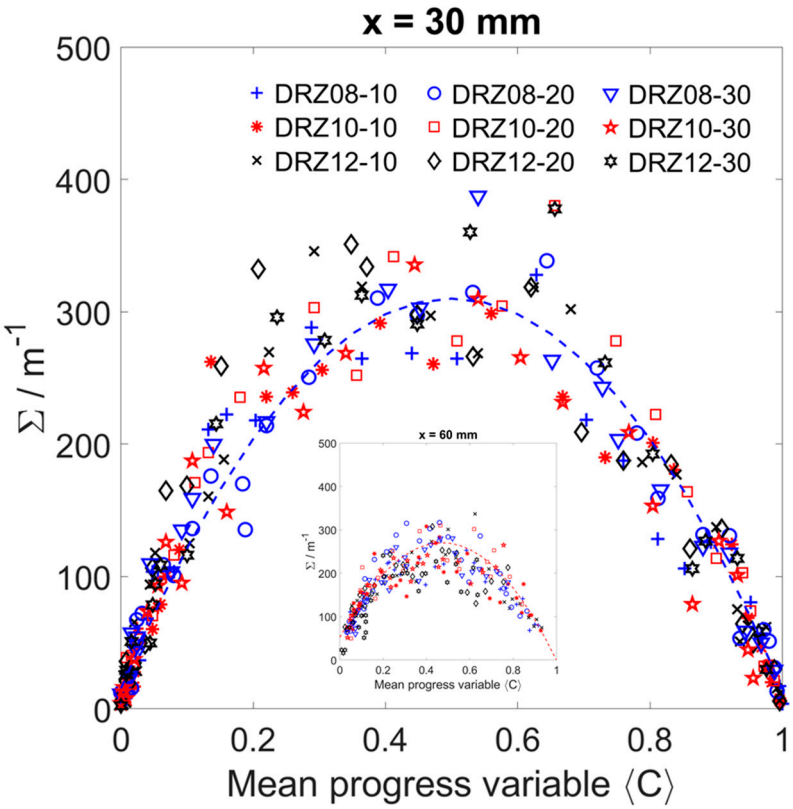

Fig. 4.22. Relation between Σ and $\langle C \rangle$ based on OH-PLIF at two flame heights for all cases. A polynomial profile fitted by the data was added.

In fact, the area ratio in Equation (4.8) can be obtained from Fig. 4.22 by calculating the area enclosed by the polynomial profile and the abscissa axis, which should be weakly dependent of the working conditions. To be more precise, the values of $A_T/\langle A \rangle$ were acquired from the OH-PLIF at the second height (40mm<x<75mm) to evaluate variation of the ratio of wrinkled flame surface area to the mean flame brush. Results are plotted in Fig. 4.23. Although the wrinkle ratio increases with the turbulent intensity, compared with the growth rate of the turbulent burning velocity in Fig. 4.20, the increase of turbulent flame surface area is not enough to explain the boost of the turbulent burning velocity. Given that in equation (4.9) another factor influences the S_T, I_0 needs more discussion.

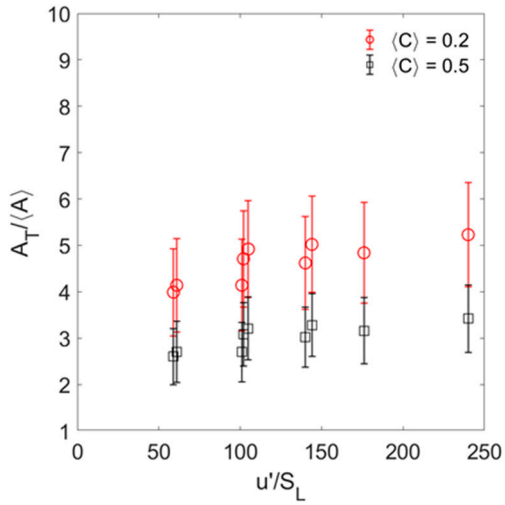

Fig. 4.23. Relation between flame surface area ratio $A_T/\langle A\rangle$ and turbulent intensity u'/S_L based on OH-PLIF from x= 40 mm to x=75 mm for all cases.

Values of the stretch factor I_0 were computed and are shown in Fig. 4.24. I_0 can be observed to increase from 2 to 6 with the u'/S_L varying from 60 to 240. The study of DNS in lean premixed methane/air flames at low turbulent intensity reported that the value of I_0 varied from 1.09 to 1.12 while u'/S_L varied from 1.7 to 4.3 [79]. This conclusion is consistent with the present results obtained by using an extrapolating function to the low values of u'/S_L. The high value of I_0 can be explained by the following factors. First, the effect of the higher flame stretch rate enhances the local displacement velocity. A recent DNS study showed that the value of I_0 can be 5 to 10 in turbulent premixed flames [80]. Second, the 2D visualisation underestimates the values of $A_T/\langle A\rangle$, not considering the 3D effect. Zhang et al. [81] found that the flame surface density in a 3D Bunsen flame can be 10% – 50% higher than the 2D one. That the flame wrinkle structure is not fully resolved by the present spatial resolution can be a third factor. The fine structures on the same order of the spatial resolution are, in essence, filtered, leading to an overestimated I_0.

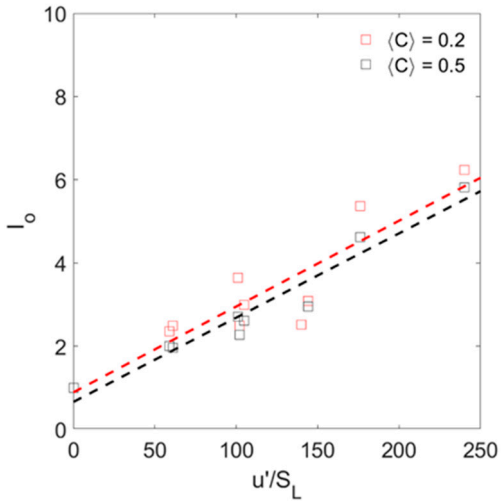

Fig. 4.24. Relation between stretch factor I_0 and turbulent intensity u'/S_L for all cases.

5 Summary and outlook

5.1 Summary

This thesis has provided deepened insight into the characteristics of premixed ammonia/air combustion under high Karlovitz number conditions. Laser-based diagnostic techniques were used to acquire fundamental knowledge from a lab-scale jet flame and a large Bunsen flame, by extension scaling to industrial-level applications. The investigated cases are located within the distributed reaction zone regime with a wide range of integral length scales and turbulent intensities. Qualitative and quantitative analysis were applied to investigate the development of the flame structures, especially of the reaction zone. Discussion of the correlation of the reactive scalars and the turbulent burning velocity was also involved in the different studies. The main conclusions are summarised below:

In the lab-scale LUPJ flames:

- The NH layer remains thin and continuous when the Ka is less than 590. However, as the turbulent intensity increases, significant broadening was observed at higher flame heights. The broadening of the NH layer is the result of the turbulence eddy/flame interaction, and local flame merger. The statistical analysis indicates that the thickness of NH layer can increase 3 – 4 times downstream in flames at Ka 1900 or greater.
- The boundary between the thin reaction zone regime and distributed reaction zone regime in the LUPJ flames is at a much higher Ka than in the methane/air flames at Ka of approx. 100 on the same burner, indicating that regime classification is also fuel related.
- The laminar ammonia/air flames show that the NO pollutant mainly forms in the reaction zone around 1500 K. However, most NO is found at lower temperatures in the corresponding turbulent flames, which suggests a strong turbulent influence on the NO field. The NO is likely transported to the preheat zone.

In the large-scale DRZ flames:

- The NH and OH radicals coexist in a thin layer under all operation conditions. The NH layer remains thin and no broadening was observed with the Ka up to 1008 with a turbulent intensity of 240. This observation suggests that the

small-scale eddies cannot penetrate the NH or fuel-consumption layers. The experimental results show that the thin reaction zone assumption may be applicable under high Karlovitz number conditions (Ka >> 100) for ammonia/air premixed flames.

- The ratio of turbulent to laminar burning velocity increases linearly with the turbulent intensity, which is consistent with the observed thin NH layer and the flamelet concept. While the analysis of the flame surface density based on the OH-PLIF indicates that flame surface wrinkling is not the dominant effect, this is contradictory to the flamelet concept. This is mainly due to the limited spatial resolution of the PLIF imaging and the difference of the flame surface density between 2D projection and 3D flame.

5.2 Outlook

This work reports the experimental studies of premixed ammonia/air combustion at high Karlovitz (Ka) number conditions. It can be regarded as the beginning of research on ammonia combustion and several research questions remain unanswered. Some of the future works suggested:

- Although the turbulent intensity and Karlovitz (Ka) number in DRZ flames are similar to industrial applications, the effects of high temperature and high pressure present in working conditions in real combustors are not considered here. It may be hard to carry out direct investigation in such harsh environments. However, preheating reactants to a certain temperature to study flame structure is possible. The Borghi-Peters regime diagram does not include a temperature dimension, which is a very important factor for turbulent premixed combustion.
- The studies were conducted on two different burners to visualise the fuel consumption layer by the NH-PLIF method, while the results demonstrate a different conclusion. The NH layer in the DRZ flames remains thin and continuous. However, broadening happens in the LUPJ flames when the Ka is higher than 1900. Similar findings were observed in previous studies of methane/air flames. A more precise regime diagram is needed, taking into consideration the burner geometries, turbulence generating mechanisms, fuel types, and other necessary parameters.
- NO emission, one of the main issues of ammonia combustion, still needs further investigations. Usually, the minimum production of NO is achieved under fuel-rich conditions, but the amount of unburnt ammonia will increase dramatically. To deepen the relevant understanding at highly turbulent intensities, the NO-PLIF can be carried out in the DRZ flames and the

concentration of this pollutant will be analysed by the emission analyser. Furthermore, ammonia leakage can be measured by two-photon laser-induced fluorescence [82] or laser-induced photofragmentation fluorescence [83]. The reduction of NO emission under highly turbulent conditions is important for combustor design.

References

[1] E.D. Coyle, R.A. Simmons, Understanding the global energy crisis, Purdue University Press 2014.

[2] IEA (2021), Global Energy Review: CO2 Emissions in 2020, IEA, Paris https://www.iea.org/articles/global-energy-review-co2-emissions-in-2020.

[3] IEA (2019), The Future of Hydrogen, IEA, Paris https://www.iea.org/reports/the-future-of-hydrogen.

[4] H. Kobayashi, A. Hayakawa, K.D.K. A. Somarathne, E. C. Okafor, Science and technology of ammonia combustion, Proceedings of the Combustion Institute 37 (2019) 109-133.

[5] M. Aziz, A.T. Wijayanta, A.B.D. Nandiyanto, Ammonia as Effective Hydrogen Storage: A Review on Production, Storage and Utilization, Energies 13 (2020) 3062.

[6] B.H. Suryanto, K. Matuszek, J. Choi, R.Y. Hodgetts, H.-L. Du, J.M. Bakker, C.S. Kang, P.V. Cherepanov, A.N. Simonov, D.R. MacFarlane, Nitrogen reduction to ammonia at high efficiency and rates based on a phosphonium proton shuttle, Science 372 (2021) 1187-1191.

[7] B. Lee, J. Park, H. Lee, M. Byun, C.W. Yoon, H. Lim, Assessment of the economic potential: COx-free hydrogen production from renewables via ammonia decomposition for small-sized H2 refueling stations, Renewable and Sustainable Energy Reviews 113 (2019) 109262.

[8] N. Peters, Turbulent combustion, Cambridge University Press, 2001.

[9] A. Ichikawa, Y. Naito, A. Hayakawa, T. Kudo, H. Kobayashi, Burning velocity and flame structure of CH4/NH3/air turbulent premixed flames at high pressure, International Journal of Hydrogen Energy 44 (2019) 6991-6999.

[10] R. Ichimura, K. Hadi, N. Hashimoto, A. Hayakawa, H. Kobayashi, O. Fujita, Extinction limits of an ammonia/air flame propagating in a turbulent field, Fuel 246 (2019) 178-186.

[11] A. Hayakawa, Y. Arakawa, R. Mimoto, K.D.K.A. Somarathne, T. Kudo, H. Kobayashi, Experimental investigation of stabilization and emission characteristics of ammonia/air premixed flames in a swirl combustor, International Journal of Hydrogen Energy 42 (2017) 14010-14018.

[12] E.C. Okafor, K.D.K.A. Somarathne, A. Hayakawa, T. Kudo, O. Kurata, N. Iki, H. Kobayashi, Towards the development of an efficient low-NOx ammonia combustor for a micro gas turbine, Proceedings of the Combustion Institute 37 (2019) 4597-4606.
[13] E.C. Okafor, K.D.K.A. Somarathne, R. Ratthanan, A. Hayakawa, T. Kudo, O. Kurata, N. Iki, T. Tsujimura, H. Furutani, H. Kobayashi, Control of NOx and other emissions in micro gas turbine combustors fuelled with mixtures of methane and ammonia, Combustion and Flame 211 (2020) 406-416.
[14] R. Li, A.A. Konnov, G. He, F. Qin, D. Zhang, Chemical mechanism development and reduction for combustion of NH3/H2/CH4 mixtures, Fuel 257 (2019) 116059.
[15] K. Seshadri, N. Peters, The inner structure of methane-air flames, Combustion and Flame 81 (1990) 96-118.
[16] R.C. Rocha, S. Zhong, L. Xu, X.-S. Bai, M. Costa, X. Cai, H. Kim, C. Brackmann, Z. Li, M. Aldén, Structure and Laminar Flame Speed of an Ammonia/Methane/Air Premixed Flame under Varying Pressure and Equivalence Ratio, Energy & Fuels, doi:10.1021/acs.energyfuels.0c03520 (2021).
[17] K.K. Kuo, Principles of combustion, 2005.
[18] T. Poinsot, D. Veynante, Theoretical and numerical combustion, RT Edwards, Inc.2005.
[19] Y.B. Zeldovich, D.A. Frank-Kamenetskii, The theory of thermal propagation of flames, Zh. Fiz. Khim 12 (1938) 100-105.
[20] E. Kessler, Thunderstorms: The Thunderstorm in human affairs, US Department of Commerce, National Oceanic and Atmospheric Administration 1981.
[21] H. Tennekes, J.L. Lumley, A first course in turbulence, MIT press2018.
[22] L.F. Richardson, Weather prediction by numerical process, Cambridge university press2007.
[23] S.B. Pope, Turbulent flows, Cambridge University Press, 2001.
[24] K.K. Kuo, R. Acharya, Fundamentals of turbulent and multiphase combustion, John Wiley & Sons, (2012).
[25] R. Borghi, On the structure and morphology of turbulent premixed flames, Recent advances in the Aerospace Sciences, Springer1985, pp. 117-138.
[26] R. Borghi, Turbulent combustion modelling, Progress in energy and combustion science 14 (1988) 245-292.
[27] Z.S. Li, B. Li, Z.W. Sun, X.S. Bai, M. Aldén, Turbulence and combustion interaction: High resolution local flame front structure visualization using simultaneous single-shot PLIF imaging of CH, OH, and CH2O in a piloted premixed jet flame, Combustion and Flame 157 (2010) 1087-1096.

[28] A.W. Skiba, T.M. Wabel, C.D. Carter, S.D. Hammack, J.E. Temme, J.F. Driscoll, Premixed flames subjected to extreme levels of turbulence part I: Flame structure and a new measured regime diagram, Combustion and Flame 189 (2018) 407-432.
[29] Y.-C. Chen, R.W. Bilger, Simultaneous 2-D Imaging Measurements of Reaction Progress Variable and OH Radical Concentration in Turbulent Premixed Flames: Experimental Methods and Flame Brush Structure, Combustion Science and Technology 167 (2001) 131-167.
[30] C. Kortschik, T. Plessing, N. Peters, Laser optical investigation of turbulent transport of temperature ahead of the preheat zone in a premixed flame, Combustion and Flame 136 (2004) 43-50.
[31] F.T.C. Yuen, Ö.L. Gülder, Dynamics of Lean-Premixed Turbulent Combustion at High Turbulence Intensities, Combustion Science and Technology 182 (2010) 544-558.
[32] R. Sankaran, E.R. Hawkes, J.H. Chen, T. Lu, C.K. Law, Structure of a spatially developing turbulent lean methane–air Bunsen flame, Proceedings of the combustion institute 31 (2007) 1291-1298.
[33] A. Aspden, M. Day, J. Bell, Three-dimensional direct numerical simulation of turbulent lean premixed methane combustion with detailed kinetics, Combustion and Flame 166 (2016) 266-283.
[34] J. Rosell, X.-S. Bai, J. Sjoholm, B. Zhou, Z. Li, Z. Wang, P. Pettersson, Z. Li, M. Richter, M. Alden, Multi-species PLIF study of the structures of turbulent premixed methane/air jet flames in the flamelet and thin-reaction zones regimes, Combustion and Flame 182 (2017) 324-338.
[35] T.M. Wabel, A.W. Skiba, J.F. Driscoll, Turbulent burning velocity measurements: Extended to extreme levels of turbulence, Proceedings of the Combustion Institute 36 (2017) 1801-1808.
[36] S.A. Filatyev, J.F. Driscoll, C.D. Carter, J.M. Donbar, Measured properties of turbulent premixed flames for model assessment, including burning velocities, stretch rates, and surface densities, Combustion and Flame 141 (2005) 1-21.
[37] Z. Wang, B. Zhou, S. Yu, C. Brackmann, Z. Li, M. Richter, M. Aldén, X.-S. Bai, Structure and burning velocity of turbulent premixed methane/air jet flames in thin-reaction zone and distributed reaction zone regimes, Proceedings of the Combustion Institute 37 (2019) 2537-2544.
[38] H. Kobayashi, K. Seyama, H. Hagiwara, Y. Ogami, Burning velocity correlation of methane/air turbulent premixed flames at high pressure and high temperature, Proceedings of the Combustion Institute 30 (2005) 827-834.
[39] G. Damköhler, The effect of turbulence on the flame velocity in gas mixtures, Z. Elektrochem. und Angewandte Physikalische Chemie 46 (1940) 601, English translation, NACA Techn. Memo. No.1112 1947.

[40] J. Driscoll, Turbulent premixed combustion: Flamelet structure and its effect on turbulent burning velocities, Progress in Energy and Combustion Science 34 (2008) 91-134.
[41] K.N.C. Bray, R. Cant, Some applications of Kolmogorov's turbulence research in the field of combustion, Proceedings of the Royal Society of London. Series A: Mathematical and Physical Sciences 434 (1991) 217-240.
[42] M.J. Dunn, A.R. Masri, R.W. Bilger, A new piloted premixed jet burner to study strong finite-rate chemistry effects, Combustion and Flame 151 (2007) 46-60.
[43] B. Zhou, C. Brackmann, Q. Li, Z. Wang, P. Petersson, Z. Li, M. Aldén, X.-s. Bai, Distributed reactions in highly turbulent premixed methane/air flames, Combustion and Flame 162 (2015) 2937-2953.
[44] B. Zhou, C. Brackmann, Z. Li, M. Aldén, X.-S. Bai, Simultaneous multi-species and temperature visualization of premixed flames in the distributed reaction zone regime, Proceedings of the Combustion Institute 35 (2015) 1409-1416.
[45] B. Zhou, C. Brackmann, Z. Wang, Z. Li, M. Richter, M. Aldén, X.-S. Bai, Thin reaction zone and distributed reaction zone regimes in turbulent premixed methane/air flames: Scalar distributions and correlations, Combustion and Flame 175 (2017) 220-236.
[46] J. Temme, T.M. Wabel, A.W. Skiba, J.F. Driscoll, Measurements of Premixed Turbulent Combustion Regimes of High Reynolds Number Flames, 53rd AIAA Aerospace Sciences Meeting, 2015.
[47] T.M. Wabel, A.W. Skiba, J.E. Temme, J.F. Driscoll, Measurements to determine the regimes of premixed flames in extreme turbulence, Proceedings of the Combustion Institute 36 (2017) 1809-1816.
[48] J.F. Driscoll, J.H. Chen, A.W. Skiba, C.D. Carter, E.R. Hawkes, H. Wang, Premixed flames subjected to extreme turbulence: Some questions and recent answers, Progress in Energy and Combustion Science 76 (2020) 100802.
[49] M.J. Dunn, A.R. Masri, R.W. Bilger, R.S. Barlow, G.H. Wang, The compositional structure of highly turbulent piloted premixed flames issuing into a hot coflow, Proceedings of the Combustion Institute 32 (2009) 1779-1786.
[50] M.J. Dunn, A.R. Masri, R.W. Bilger, R.S. Barlow, Finite Rate Chemistry Effects in Highly Sheared Turbulent Premixed Flames, Flow, Turbulence and Combustion 85 (2010) 621-648.
[51] S. Mohammadnejad, Q. An, P. Vena, S. Yun, S. Kheirkhah, Thick reaction zones in non-flamelet turbulent premixed combustion, Combustion and Flame 222 (2020) 285-304.

[52] T.M. Wabel, A.W. Skiba, J.F. Driscoll, Evolution of turbulence through a broadened preheat zone in a premixed piloted Bunsen flame from conditionally-averaged velocity measurements, Combustion and Flame 188 (2018) 13-27.
[53] A.J. Aspden, M.S. Day, J.B. Bell, Towards the distributed burning regime in turbulent premixed flames, Journal of Fluid Mechanics 871 (2019) 1-21.
[54] S. Lapointe, B. Savard, G. Blanquart, Differential diffusion effects, distributed burning, and local extinctions in high Karlovitz premixed flames, Combustion and Flame 162 (2015) 3341-3355.
[55] H. Wang, E.R. Hawkes, B. Zhou, J.H. Chen, Z. Li, M. Aldén, A comparison between direct numerical simulation and experiment of the turbulent burning velocity-related statistics in a turbulent methane-air premixed jet flame at high Karlovitz number, Proceedings of the Combustion Institute 36 (2017) 2045-2053.
[56] B. Zhou, J. Kiefer, J. Zetterberg, Z. Li, M. Aldén, Strategy for PLIF single-shot HCO imaging in turbulent methane/air flames, Combustion and Flame 161 (2014) 1566-1574.
[57] A. Hayakawa, T. Goto, R. Mimoto, T. Kudo, H. Kobayashi, NO formation/reduction mechanisms of ammonia/air premixed flames at various equivalence ratios and pressures, Mechanical Engineering Journal 2 (2015) 14-00402-00414-00402.
[58] R.W.B. Pearse, A.G. Gaydon, R.W.B. Pearse, A.G. Gaydon, The identification of molecular spectra, Chapman and Hall London1976.
[59] T.M. Wabel, An experimental investigation of premixed combustion in extreme turbulence, Ph. D. Thesis, (2017).
[60] X. Liu, M. Bertsch, A.A. Subash, S. Yu, R.-Z. Szasz, Z. Li, P. Petersson, X.-S. Bai, M. Aldén, D. Lörstad, Investigation of turbulent premixed methane/air and hydrogen-enriched methane/air flames in a laboratory-scale gas turbine model combustor, International Journal of Hydrogen Energy 46 (2021) 13377-13388.
[61] A.C. Eckbreth, Laser diagnostics for combustion temperature and species, CRC press1996.
[62] J.W. Daily, Laser induced fluorescence spectroscopy in flames, Progress in energy and combustion science 23 (1997) 133-199.
[63] R. Wellander, M. Richter, M. Aldén, Time-resolved (kHz) 3D imaging of OH PLIF in a flame, Experiments in Fluids 55 (2014).
[64] L. Ma, Q. Lei, T. Capil, S.D. Hammack, C.D. Carter, Direct comparison of two-dimensional and three-dimensional laser-induced fluorescence measurements on highly turbulent flames, Opt Lett 42 (2017) 267-270.
[65] X. Liu, Experimental studies of turbulent flames at gas turbine relevant burners and operating conditions, Lund University2021.

[66] A.D.P.R. Shardanand, Absolute Rayleigh scattering cross sections of gases and Freons of stratospheric interest in the visible and ultraviolet regions, NASA Tech.Rep. TN D-8442 (National Aeronautics and Space Administration, Washington, D.C.), (1981).
[67] A. Skiba, On the Structure of Premixed Flames Subjected to Extreme Levels of Turbulence (Doctoral dissertation), Michigan University, 2017.
[68] J.S. Lim, Two-dimensional signal and image processing, Englewood Cliffs, (1990) pp. 469-476.
[69] N. Otsu, A threshold selection method from gray-level histograms, IEEE transactions on systems, man, cybernetics 9 (1979) 62-66.
[70] D. Bradley, G. Roth, Adaptive thresholding using the integral image, Journal of graphics tools 12 (2007) 13-21.
[71] F. Meyer, Topographic distance and watershed lines, Signal Processing 38 (1994) 113-125.
[72] R.C. Rocha, M. Costa, X.-S. Bai, Combustion and Emission Characteristics of Ammonia under Conditions Relevant to Modern Gas Turbines, Combustion Science and Technology, doi:10.1080/00102202.2020.1748018(2020) 1-20.
[73] C. Brackmann, B. Zhou, Z.S. Li, M. Aldén, Strategies for Quantitative Planar Laser-Induced Fluorescence of NH Radicals in Flames, Combustion Science and Technology 188 (2016) 529-541.
[74] E.C. Okafor, Y. Naito, S. Colson, A. Ichikawa, T. Kudo, A. Hayakawa, H. Kobayashi, Experimental and numerical study of the laminar burning velocity of CH4–NH3–air premixed flames, Combustion and Flame 187 (2018) 185-198.
[75] G. Heskestad, A generalized Taylor hypothesis with application for high Reynolds number turbulent shear flows, (1965).
[76] C.M. García, M.H. García, Characterization of flow turbulence in large-scale bubble-plume experiments, Experiments in Fluids 41 (2006) 91-101.
[77] U. Grenander, The Nyquist frequency is that frequency whose period is two sampling intervals, Probability and Statistics: The Harald Cramér Volume, (1959) 434.
[78] P. Domingo, L. Vervisch, S. Payet, R. Hauguel, DNS of a premixed turbulent V flame and LES of a ducted flame using a FSD-PDF subgrid scale closure with FPI-tabulated chemistry, Combustion and Flame 143 (2005) 566-586.
[79] J.B. Bell, M.S. Day, J.F. Grcar, Numerical simulation of premixed turbulent methane combustion, Proceedings of the Combustion Institute 29 (2002) 1987-1993.
[80] F. Pignatelli, R. Yu, X.-S. Bai, K.-J. Nogenmyr, Displacement speed analysis of surface propagation in moderately turbulent premixed reacting waves, Physics of Fluids 33 (2021) 035109.

[81] M. Zhang, J. Wang, W. Jin, Z. Huang, H. Kobayashi, L. Ma, Estimation of 3D flame surface density and global fuel consumption rate from 2D PLIF images of turbulent premixed flame, Combustion and Flame 162 (2015) 2087-2097.
[82] C. Brackmann, O. Hole, B. Zhou, Z.S. Li, M. Aldén, Characterization of ammonia two-photon laser-induced fluorescence for gas-phase diagnostics, Applied Physics B 115 (2014) 25-33.
[83] W. Weng, C. Brackmann, M. Aldén, Z. Li, Planar laser-induced photofragmentation fluorescence for quantitative ammonia imaging in combustion environments, Combustion and Flame, (2021) 111687.

Acknowledgements

Finally, the acknowledgements. I cannot believe how quickly four years passed. It is crazy to recall the moment when I arrived in Lund, August 31, 2017. You cannot write something better than this opportunity to pursue my PhD and work in our division. My journey must be the most precious treasure in my memory.

First, I would like to thank my main supervisor, Prof. Zhongshan Li. Thank you for being open and comprehensive in our discussions. Every meeting we had remains clear and distinct in my mind. From offering an available lab for experiments, to sharing places with colleagues on vacation, to fixing a solid-state Alexandrite laser, to optimizing the dye laser, to my first draft, which you tried hard to understand, I am so proud of overcoming these funny and difficult research issues to achieve our goal at last. I have been inspired by the countless hours you spent in your office, and the attitude you take to reject 'lying-flatism'.

I would like to thank my co-supervisor, Prof. Marcus Aldén. Thank you for providing me the opportunity to become involved in different projects. You are an amazing leader and a true scientist as well. Building such a world-class research team and keeping it running for thirty years, you have completed an impossible task. Your spirit has attracted and inspired me.

Special thanks should be given to Prof. Xue-Song Bai. I sincerely appreciate that you spent a great deal of time and effort on my work. Without your help and advice, I would not have finished this thesis. Thank you for your patient and professional guidance. I have gained deep knowledge of turbulent combustion from your courses, our discussions, and zoom meetings. The whole process was enjoyable and memorable. Thank you again, from the bottom of my heart.

I also want to express my gratitude to Dr. Christian Brackmann. Thank you for sharing the lab with me for several months, even though your project has not been finished. Thank you for the countless times you taught me to align and optimise the lasers. I have learned much and acquired skills from you during the laser operations. You were careful and patient with me, although you look so serious at work ☺. I will always regard you as another co-supervisor.

Many thanks to all the people who helped my work during the past four years. I cannot forget the days and nights working with Dr. Xiao Cai during the first half of 2020. The moment when we shared a small mix bucket at 10 p.m. in the kitchen

is memorable. I wish you all the best in Xi'an. Thanks to Dr. Arman Ahamed Subash, who strengthened my experimental safety awareness. I really appreciate the time we worked together in the low swirl lab. The LDA measurement proceeds so smoothly because of the frequent contact you made with Dantec. The people who lent me equipment are wonderful: Maria Ruchkina, Yupan Bao, Dr. Pengji Ding, Dr. Andreas Ehn, Dr. Dina Hot, Dr. Per Samuelsson, Ruike Bi, Saeed Derafshzan, David Sanned, Dr. Manu Mannazhi, Dr. Marco Lubrano Lavadera, Haisol Kim, Dr. Magnus Joelsson. Thanks also to Minna Ramkull, Cecilia Bille, Igor Buzuk, Johan Evers, Dr. Robert Collin, and Dr. Sven-Inge Möller for the support and help in our division.

I am grateful to my friends, Dr. Wubin Weng, Dr. Mengshu Hao, Shen Li, Dr. Zhenkan Wang, Jie Zhong, Yupan Bao, Yingzhe Xiong, Dr. Jinlong Gao, Dr. Zhen Li, Dr. Chengdong Kong, Jie Niu, Lai Wei, Dr. Shichao Ren, Dr. Rui Li, Dr. Jian Wu, Dr. Pengji Ding, Dr. Xiao Cai, Dr. Yong Qian, Dr. Xinlu Han, Ruike Bi, Jianqing Huang, Yuhe Zhang, Zhiyong Wu, Kailun Zhang, Meng Li, Dr. Christoffer Pichler, Dr. Joakim Jönsson, Leonardo Padial, etc. and to those in Lund, Dr. Senbin Yu, Dr. Miao Zhang, Dr. Shijie Xu, Dr. Miao Yang, Dr. Leilei Xu, Dr. Kena Li, Jixing Ding, Dr. Haoran Yu, Dr. Qi Shi, Dr. Juanzi Shi, Dr. Haiyue Gong, Wenjun Wen, Dr. Huiting Ma, Yi Yang, Ye Shui, etc. Thanks for making my PhD life interesting and wonderful.

I also want to give special thanks to my friends in China, especially classmates in the "554" wechat group: Dr. Chong Zhong, Zheyuan Zhang, Xiong Yang, and Dr. Mingyang Zhang. Thank you for playing auto-chess with me when I feel work is boring. Thank you for your suggestions about my future career. I wish all of you the best of life, and hope we can get together soon.

I am extremely grateful to my parents. Thanks for your love, support, and encouragement at every stage of my growth. I also want to give my special thanks to other family members, uncles, aunts, cousins and parents-in-law, who are always caring and supporting me.

Last, but not least, my deepest gratitude to my wife, Xin Liu. Thank you for your company since 2013. Thank you for preparing everything well when I came here. It was really a challenge for you to stay alone in Sweden for almost one year. You are a true warrior. Thank you for your dedication to this family.

Summary of papers

Paper I

Q. S. Fan, X. Liu, L. L. Xu, A. A. Subash, C. Brackmann, M. Aldén, X. S. Bai and Z. S. Li, "Flame structure and burning velocity of ammonia/air turbulent premixed flames at high Karlovitz number conditions", *Manuscript submitted to* Combustion and Flame*, 2021.*

I designed the burner and planned the experiment. X. Liu and I conducted the measurements. I did all the data processing. I wrote the manuscript with help from X. S. Bai.

Paper II

Q. S. Fan, X. Liu, X. Cai, C. Brackmann, M. Aldén, X. S. Bai and Z. S. Li, "Structure and scalar correlation of ammonia/air turbulent premixed flames in the distributed reaction zone regime", *Manuscript submitted to* Combustion and Flame*, 2021.*

I planned the experiment and carried out the measurements together with X. Cai. I did all the data processing. I wrote the manuscript with help from X. S. Bai.

Paper III

X. Cai, **Q. S. Fan**, X. Liu, C. Brackmann, W. Weng, J. Wang, Z. Huang, M. Aldén, X. S. Bai and Z. S. Li, "Role of differential diffusion in the structure of premixed ammonia/hydrogen/air flames in the distributed reaction zone regime", *Manuscript submitted to* Combustion and Flame*, 2021.*

I planned the experiment and carried out the measurements together with X. Cai. I did most of the data processing.